



Cite this: *J. Mater. Chem. C*, 2019,
7, 9782

Perspectives and challenges in multilayer ceramic capacitors for next generation electronics

Kootak Hong,^{†[a](#)} Tae Hyung Lee,^{†[a](#)} Jun Min Suh, ^a Seok-Hyun Yoon*^b and Ho Won Jang ^a

The multilayered ceramic capacitor (MLCC) is a key component of electronic equipment, such as smartphones, portable PCs and electric vehicles, which contain a number of MLCCs. As MLCCs distribute and control the amount of current flowing through circuits, remove noise, and prevent malfunction, MLCCs play a key role in enabling electronic devices to have high performance, multi-functionality, and high integration. This review highlights the critical issues and recent progress in developing highly volumetric-efficient and high capacitance MLCCs from the viewpoint of designing a BaTiO₃-based dielectric layer. After a brief introduction of MLCCs and dielectric materials, we summarize the current issues in developing BaTiO₃-based dielectric materials for MLCCs with high performance and reliability and describe the strategies to optimize dielectric properties through nano/microstructure control, chemical modification and doping. Finally, we provide an outlook on the development and future application of MLCCs. It is anticipated that this review can serve as an overview and evaluation of state-of-the-art synthesis and design of BaTiO₃-based dielectric materials for MLCC applications.

Received 31st May 2019,
Accepted 12th July 2019

DOI: 10.1039/c9tc02921d

rsc.li/materials-c

1. Introduction

As known from words such as digital nomad, ubiquitous computing, and internet of things, there have been growing needs for electronic devices that are portable and can be connected to a network with high speed and transmission capacity. Due to

these trends, miniaturization, research on high performance, high reliability, and low electric power consumption of electronic components has been accelerated. Among them, the multilayer ceramic capacitor (MLCC) is the most important passive component which can store and release electrical charge. MLCCs offer high stability and low losses for resonant circuit applications and high volumetric efficiency for buffer, by-pass, and coupling applications.^{1–4}

Recently, the global MLCC shortage has become a major issue due to the increase in demand for MLCCs in smartphones, portable PCs and the automotive industry. This is because the increase in demand from these markets has been

^a Department of Materials Science and Engineering, Research Institute of Advanced Materials, Seoul 08826, Republic of Korea. E-mail: hwjang@snu.ac.kr

^b LCR Materials Group, Corporate R&D Institute, Samsung Electro-Mechanics Co., Ltd, Suwon, Gyeonggi-Do 16674, Republic of Korea.

E-mail: seokhyun72.yoon@samsung.com

† These authors contributed equally to this work.



Kootak Hong is a postdoctoral research fellow at the Department of Materials Science and Engineering, Seoul National University (SNU). He received his BS and PhD degrees from the Department of Materials Science and Engineering of SNU in 2013 and 2018, respectively. His current research interests focus on nanoelectronics in oxide semiconductors and their applications.



Tae Hyung Lee

Tae Hyung Lee is currently a PhD candidate in the Department of Materials Science and Engineering at Seoul National University (SNU). He received his BS degree from the Department of Materials Science and Engineering, SNU, in 2016. His research is focused on oxide semiconductors and their application combined with theoretical study based on first principles calculations.

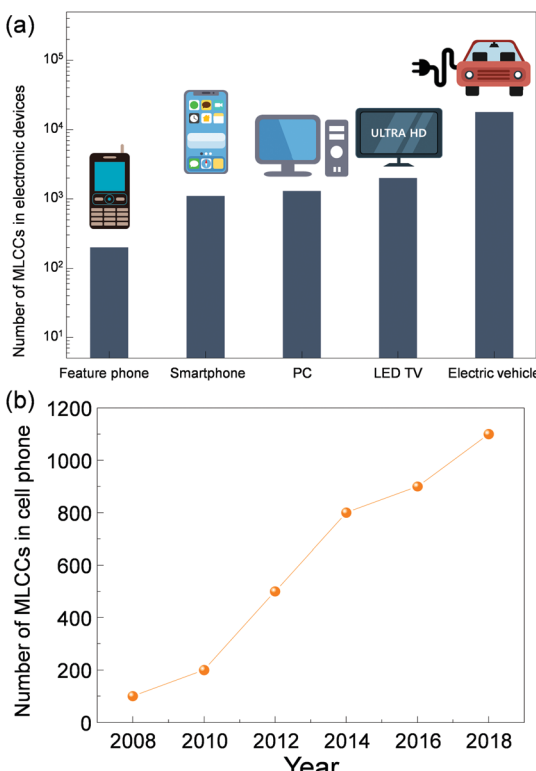


Fig. 1 (a) The number of MLCCs contained in different electronic equipment. (b) Annual increase of MLCCs used in mobile phones.

significantly higher than the manufacturers expected. As shown in Fig. 1a, the electronic devices, which we use every day, such as smartphones, computers and LED TVs, contain more than 1000 MLCCs.⁵ For electric vehicles, more than 10 000 MLCCs are needed for their electronic control and automation system. As MLCCs distribute and control the amount of current flowing



Seok-Hyun Yoon

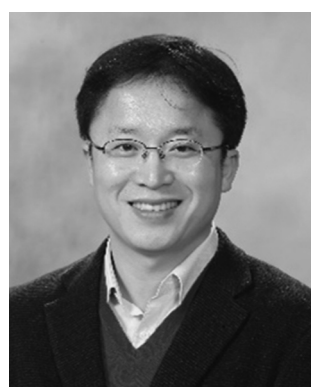
Pennsylvania State University from 2008 to 2010. His research interests include ferroelectric phenomena, defect chemistry, electrical conduction, sintering, and ceramic processes that are related with the dielectric materials of capacitors.

Seok-Hyun Yoon is a Group Leader of MLCC Materials Development of the Corporate R&D Institute of Samsung Electro-Mechanics. He received his PhD from the Department of Materials Science and Engineering at Seoul National University in 2001. Before he joined Samsung in 2003, he worked as a Senior Researcher at Center for Microstructure Science & Materials of SNU. He also worked as a visiting scientist at the Center for Dielectric Studies in The

through circuits, remove noise, and prevent malfunction of electronic devices, a number of MLCCs are mounted on electronic devices. Moreover, electronic devices with high performance, multi-functionality, and high integration require large numbers of MLCCs with high capacitance. It can be known from the number of MLCCs contained in mobile phones year-on-year (Fig. 1b). The number of MLCCs used in mobile phones has grown nearly 10 times from 2008 to 2018 because smartphones have become popular and the demand for high-performance smartphones has increased.⁶

In this trend, miniaturization of MLCCs with high capacitance is a key issue, because there is limited space inside the electronic equipment due to batteries and ICs.³ Currently, MLCCs with several hundreds of dielectric layers below 1 μm have already been developed and commercialized. The mainly used case sizes specified by Electrical Industry Alliance are EIA0603 (0.6 mm × 0.3 mm) for general electronic equipment and EIA0402 (0.4 mm × 0.2 mm) for mobile electronic equipment.⁴ The MLCC with EIA 0201 (0.2 mm × 0.1 mm) will be put into practical use soon. The key factors for the development of highly volumetric efficient and high capacitance MLCCs are (i) using dielectric materials with high dielectric permittivity, (ii) stacking more dielectric layers, (iii) increasing the overlapped area of internal electrodes and (iv) reducing the thickness of the dielectric layer. For higher capacitance and volume-efficiency, the next generation MLCCs should have a greater number of stacked dielectric layers as thin as 1 μm or less. However, when dielectric layers, mainly BaTiO₃, in MLCCs become thinner, there are several problems related to the performance and reliability of MLCCs due to sintering shrinkage behavior and high electric field across the dielectric layer. Therefore, there have been many efforts to solve these problems by designing dielectric materials.^{3,4,7–15}

In this review, we aim at presenting recent breakthroughs in the design of dielectric materials for next generation MLCCs. We begin with a brief introduction to MLCCs and BaTiO₃, the



Ho Won Jang

Ho Won Jang is an Associate Professor of the Department of Materials Science and Engineering in Seoul National University. He earned his PhD from the Department of Materials Science and Engineering in Pohang University of Science and Technology in 2004. He worked as a Research Associate at University of Wisconsin-Madison from 2006 to 2009. Before he joined Seoul National University in 2012, he worked in Korea Institute of Science and Technology as a Senior Research Scientist. His research interests include the synthesis of oxides, 2D materials, and halide perovskites, and their applications for nanoelectronics, solar water splitting cells, chemical sensors, plasmonics, metal-insulator transition, and ferroelectricity.

most commonly used dielectric material in MLCCs. Next, we will review critical issues in developing the next-generation MLCCs. Additionally, recent progress and strategies to improve the performance of MLCCs from a material engineering viewpoint are summarized and discussed. Finally, we conclude this topic and provide an outlook on the development and future application of MLCCs. We hope this review can provide readers with a comprehensive overview of MLCCs and promote the development of next generation MLCCs.

2. MLCC and its fabrication process

The schematic diagram of the detailed structure of MLCCs and the fabrication procedure of MLCCs is illustrated in Fig. 2. MLCCs consist of many dielectric layers and inner electrodes which are alternately stacked in parallel. The inner electrodes are connected to the outer terminal for surface mounting. Recently, base metals, such as Ni and Fe, are mainly used as inner electrode materials by replacing expensive Pd and the outer termination is composed of a Cu or Ag layer, Ni plating layer, and Sn plating layer. The capacitance of MLCCs can be expressed as

$$C = \varepsilon_r \varepsilon_0 \frac{(n - 1)A}{d} \quad (1)$$

where ε_r is the relative dielectric permittivity, ε_0 is the vacuum permittivity, n is the number of stacked inner electrodes, A is the overlapped area of the internal electrode and d is the thickness of the dielectric layer. For MLCCs with high capacitance, the thickness of the dielectric layer and the number of stacked layers become key design factors, when the chip size and the dielectric materials are determined.

MLCCs are generally fabricated by the following method. First, fine ceramic powders for dielectric layers are homogeneously mixed with a binder, solvents, and additives, such as dopants and sintering aids, using the balling method. The composition of starting materials is precisely controlled for

better performance and reliability of MLCCs. The mixtures are in a slurry form which is easy to handle and process. Using a tape casting method, the slurry is cast into a thin, continuous sheet. After drying and cutting into equal-sized sheets, the green sheets are screen printed with a metal paste. The required number of green sheets are stacked with inner electrodes slightly offset from each other, and then, pressure is applied to the stacked green sheets to laminate them. The laminated sheets are cut into the desired chip size. For stacking and cutting, a high precision of alignment and mechanical processes is required. After cutting, the binder in the chips is burned out, and subsequently, the chips are sintered. As the chips have a multilayered structure of dielectric layers and inner electrodes, it is important to control the sintering temperature and the ambient conditions to avoid sintering shrinkage and failures. To connect the internal electrodes in parallel, termination is made on the chip through tumbling, dipping and firing processes. After electrical testing for quality, the fabrication of MLCC chips is completed.

There are several issues in the fabrication process of high capacitance MLCCs. For thinner and smoother dielectric layers and inner electrode layers, fine raw powders (< 300 nm) are required. Therefore, the synthesis of small particles for the dielectric layer and the metal inner electrode has been intensively researched. The control of sintering temperature is also important to fabricate MLCCs because high sintering temperature (> 1200 °C) of dielectric materials causes metal diffusion into the dielectric layer, residual stress and mechanical cracking due to sintering shrinkage, which result in poor performance, reduced reliability and malfunction of electrode materials of MLCCs. Additionally, to prevent the oxidation of the base metal inner electrode, the green chips are co-fired under low oxygen pressure. A significant composition change and defect formation can occur in dielectric layers during sintering under a reducing atmosphere. Hence, to prevent the reduction of the dielectric material and to limit the oxidation of the inner electrodes, the sintering atmosphere should be controlled precisely.

3. Why BaTiO₃?

From eqn (1) it is clear that MLCCs have a higher capacitance value when using dielectric materials with higher ε_r . For practical applications, MLCCs should show reliable operation with high capacitance from -55 to 150 °C according to the EIA standard (Table 1). As ferroelectric materials show the maximum value of ε_r at the Curie temperature, we plotted the dielectric permittivity *versus* the Curie temperature of ferroelectric materials in Fig. 3.^{16–28} The Curie temperature of many ferroelectric materials is above 150 °C, which is beyond the EIA standard. In the range of -55 and 150 °C, PMN-PT and BaTiO₃ have a relatively high value of ε_r compared to others. However, PMN-PT is not an appropriate candidate for dielectric materials for MLCCs because of the volatilization of the Pb metal and the reaction with base metal electrodes during sintering under a reducing atmosphere. In addition, there are environmental issues due to its toxicity.^{29–32} Therefore, considering the dielectric permittivity and operation

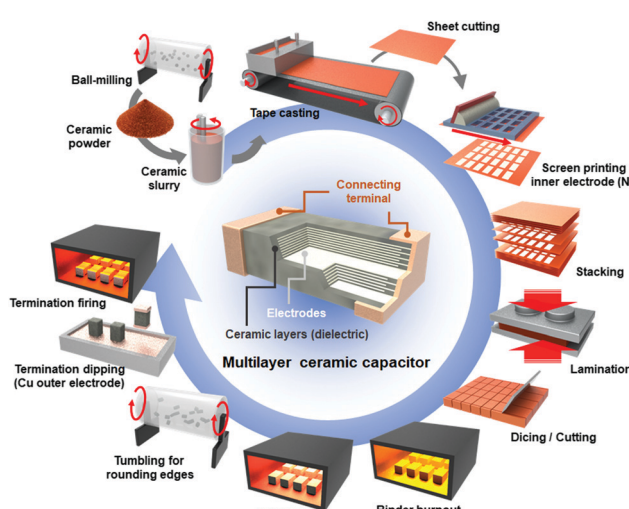
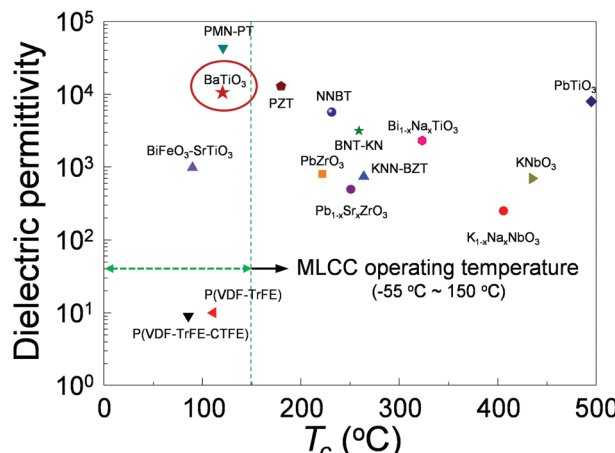


Fig. 2 Schematics of the MLCC architecture and its fabrication process.

Table 1 Electrical Industry Alliance specification codes for class II MLCCs

Letter code low temperature	Number code upper temperature	Letter code change of capacitance over the temperature range
X = -55 °C	4 = +65 °C	P = ±10%
Y = -30 °C	5 = +85 °C	R = ±15%
Z = +10 °C	6 = +105 °C	L = ±15%, +15/-40% above 125 °C
	7 = +125 °C	S = +22%
	8 = +150 °C	T = +22/-33%
	9 = +200 °C	U = +22/-56%
		V = +22/-82%

**Fig. 3** The dielectric permittivity and Curie temperature of various ferroelectric materials.^{16–28}

temperature, BaTiO₃ is the most suitable candidate, and conventional MLCCs that have been fabricated are based on BaTiO₃.

BaTiO₃ is known as the first perovskite oxide in which ferroelectric property was observed. For pure BaTiO₃, a non-linear dielectric behavior with 3 distinct peaks is observed due to the phase transition from rhombohedral to orthorhombic (−90 °C), from orthorhombic to tetragonal (0 °C) and from tetragonal to cubic (120 °C). Therefore, the composition of BaTiO₃ layers is precisely controlled in commercial MLCCs using a solid solution method or by doping in order to shift and broaden the ε_r peaks of BaTiO₃ from the Curie temperature (120 °C) to room temperature and achieve the temperature stability of ε_r .^{33,34}

The dielectric properties of BaTiO₃ can also be modified through the formation of the core–shell grain structure.^{1,3,35–37} As diffusion of the dopant occurs during the sintering process, the grains of dielectric layers in MLCCs have a pure BaTiO₃ core in which tetragonal and cubic structures co-exist and a shell formed by diffusion additives in BaTiO₃. Due to the combined dielectric behavior of the core–shell structure, low temperature capacitance change and low dielectric losses can be realized. In addition, the dielectric layers with a core–shell grain structure show high reliability and low conductivity of the dielectric layer because dopant-rich grain boundaries hinder the ionic migration of oxygen vacancies.

Recently, the BaTiO₃ dielectric layers have become thinner and thinner for highly volumetric-efficient MLCCs with high capacitance. In this trend, there are some problems in the

performance and reliability of BaTiO₃-based MLCCs. This is because as the electric field across the dielectric layer becomes higher, the dielectric properties and reliability of BaTiO₃-based MLCCs will be severely affected by voltage.^{38–40} In addition, the grain size of BaTiO₃ should be smaller (<1 μm) for thinner dielectric layers, and the dielectric properties of BaTiO₃ are seriously dependent on grain size, especially in the submicron size.^{41–44} Therefore, many researchers have paid attention to solve these problems and to understand the dielectric properties of BaTiO₃ depending on size, doping, and electric field.⁴⁴ In the following section, we will carefully review the critical issues and recent progress in developing MLCCs with high volumetric efficiency and capacitance from the point of designing the BaTiO₃-based dielectric layer.

4. Critical issues and strategies

4.1. Control of particle size and grain effects on BaTiO₃ thin films

The dielectric properties of ferroelectric materials are closely related to the crystal structure, particle size, and grain size. Such a phenomenon is named as the size effect in ferroelectric materials and this size effect has become more and more important recently with the application of nanostructured ferroelectric materials. As the size of MLCCs becomes smaller, it becomes crucial to find a way to enhance the dielectric properties of ferroelectric thin films. To control the size effect on dielectric properties, a careful investigation of the size effect and its mechanism is needed.

In Fig. 4a, the permittivity of BaTiO₃ with various particle sizes at room temperature is presented. As the particle size increases, the permittivity also increases until the size reaches 140 nm. After the optimal size of 140 nm, the permittivity starts to decrease drastically and eventually reaches a saturated value around 2000.⁷ Such a change of permittivity with size can be explained with the structure of the BaTiO₃ particle. When the BaTiO₃ particle is constructed, it can be divided into 3 parts, the surface layer with the cubic crystal structure, the inner core with the tetragonal crystal structure and the gradient lattice strain layer (GLSL) between them.^{41,43} It is commonly known that cubic BaTiO₃ shows paraelectricity while tetragonal BaTiO₃ has strong ferroelectricity. The GLSL region in BaTiO₃ has the structure between cubic and tetragonal and has relatively soft ferroelectricity when compared to tetragonal BaTiO₃. Due to the different dielectric behaviour between layers in the particle, the permittivity is closely related to the volume fraction of 3 different layers. The thickness of the cubic surface layer is almost constant with a value of 15–20 nm, regardless of the particle size. On the other hand, the GLSL and tetragonal core thickness increases as the particle size becomes large. When the particle size is small, the particle is mainly composed of the surface cubic layer, which leads to low permittivity owing to its paraelectricity. When the particle size becomes larger, the portion of the GLSL and tetragonal core, which has ferroelectricity, becomes bigger, resulting in an increase of permittivity.

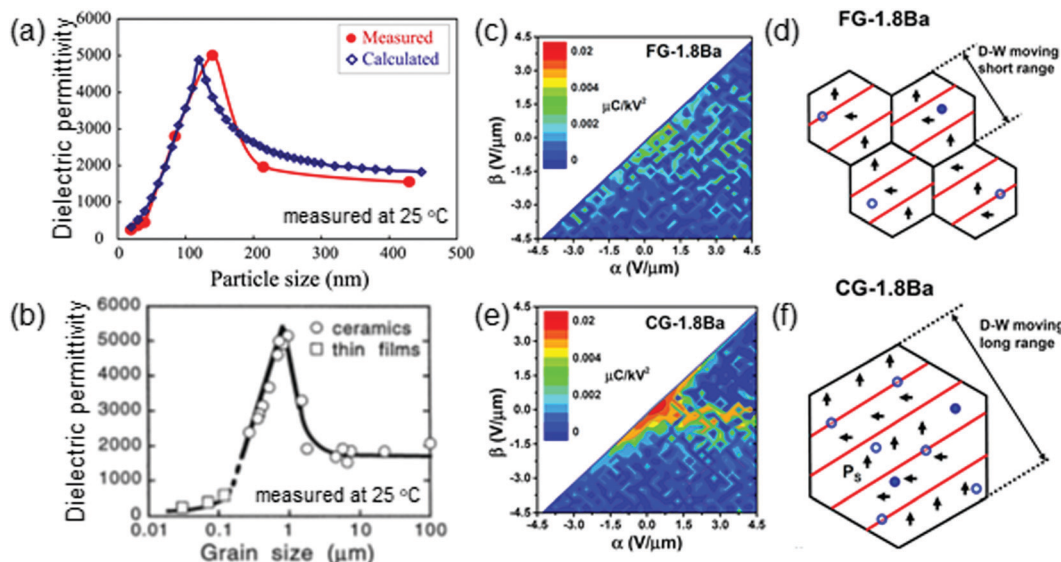


Fig. 4 (a) Dielectric permittivity of BaTiO_3 with various particle sizes at room temperature. Reproduced with permission from ref. 7. (b) Grain size dependence of the dielectric permittivity of the BaTiO_3 ceramic and thin films at room temperature. Reproduced with permission from ref. 69. The irreversible FORC distribution and schematic diagram of the supposed domain structure. (c and d) 1.8 mol% Ba-doped BaTiO_3 with fine grains. (e and f) 1.8 mol% Ba-doped BaTiO_3 with coarse grains. Reproduced with permission from ref. 8.

However, when the particle grows over 140 nm, the fraction of GLSL increases faster than the tetragonal core and becomes dominant in the particle. The relatively soft ferroelectricity of GLSL contributes to the reduction of permittivity of BaTiO_3 particles.

According to the study of Yan *et al.*, a relationship between particle size and tetragonality is also identified.⁴² By controlling the calcination temperature, they synthesized BaTiO_3 nanoparticles with the size range from 30 nm to 500 nm and characterized them by X-ray diffraction (XRD) and Raman spectroscopy analysis. From these characterization studies, it was possible to figure out that with the size increment, the tetragonality of the particle increases.

Fig. 4b shows the grain size dependency of the dielectric permittivity in BaTiO_3 thin films at room temperature. Similar to the particle size dependent permittivity, the dielectric permittivity increases until the grain size is around 1 μm and then decreases.⁴⁴ There have been several different models to explain this phenomenon. Buessem *et al.* reported that the internal stress due to the absence of 90° domain walls in fine grain BaTiO_3 leads to enhancement in dielectric permittivity,⁴⁵ while some other studies reported that fine grain size leads to stronger domain wall contribution to dielectric response.^{46,47} Also, R. Waser mentioned that below a grain size of 10 μm , the grain size has an influence on the temperature of the BaTiO_3 phase transition, especially the tetragonal–cubic transition which can affect the dielectric property.⁴⁸

As shown in Fig. 4e and e, Yoon and coworkers reported the irreversible first order reversal curve (FORC) distributions of Mn, V-doped BaTiO_3 -based MLCCs, which have fine and coarse grains. The authors used the BaTiO_3 with excess Ba concentration due to tetragonality and the magnitude of spontaneous polarization. This is because, for the dopant incorporated

ABO_3 , its structure can be changed from A-site deficient to stoichiometric and then B-site deficient ABO_3 depending on the Ba concentration.⁴⁹ As the magnitude of the spontaneous polarization is maximum at a Ba/Ti ratio of 1, excess Ba concentration is required to bring the Ba/Ti ratio of the acceptor-doped BaTiO_3 close to 1. To obtain the FORC distribution, the increasing minor hysteresis curves starting from different input values, which are called reversal points (β), to the positive saturation have to be measured. From the second-order mixed derivative of the impedance value with respect to the reversal (β) and measured field values (α), the mathematical hysteron distribution, named the FORC distribution function, is obtained.^{50,51} Irreversible FORC distribution is associated with the contribution of the irreversible domain wall motion. Comparing Fig. 4c and e, it is possible to observe that the intensity increases at the origin when the grain size becomes coarse. The difference in the irreversible contribution of domain wall motion can be explained with Fig. 4d and f, which depicts the grain of fine grain and coarse grain BaTiO_3 , respectively. The size and area of the domain wall are proportional to the grain size. The coarse grain has a larger number of pinning centers inside, and domain wall pinning occurs more easily compared to the fine grain. Under a low AC field, the pinning will disturb the domain wall motion. However, when a higher field is applied, the domain wall motion initiates resulting in an abrupt rise of dielectric permittivity with an increment of the AC field.⁸

The grain size effects can be observed in the resistance degradation behaviour as well as dielectric properties. In Fig. 5a, the conductivity in a grain of Mg-doped BaTiO_3 with various concentrations is presented. It is easily distinguished that Mg-doped BaTiO_3 with a fine grain (0.8 μm) has lower conductivity when compared with a coarse grain (90 μm) of

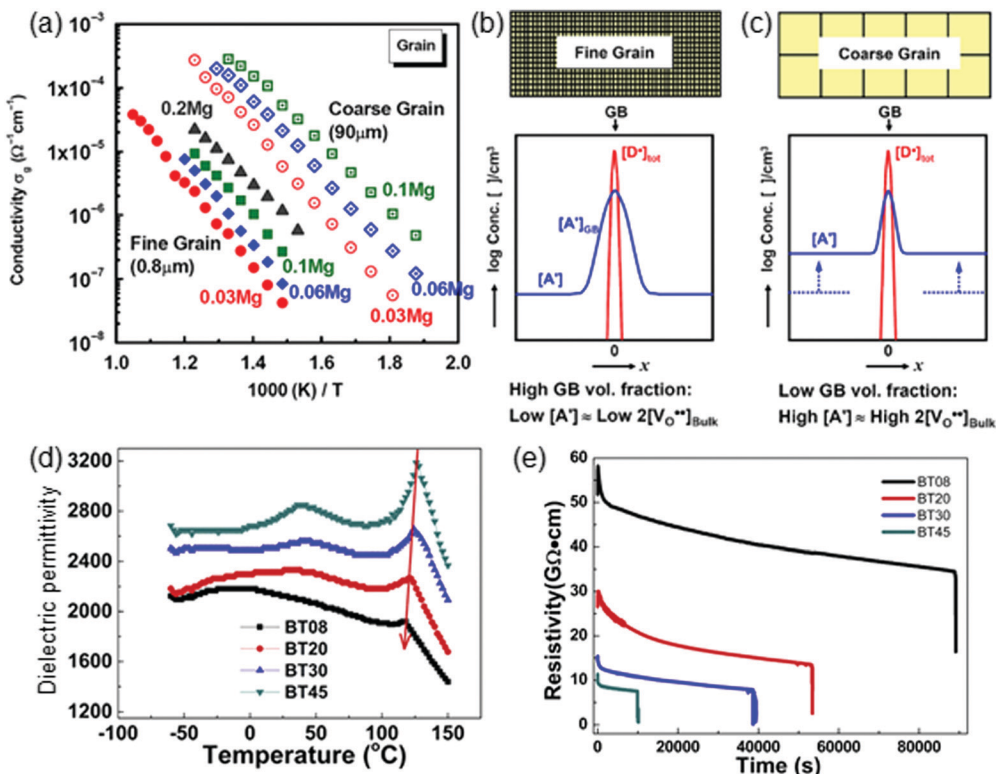


Fig. 5 (a) Temperature dependent grain conductivity of the coarse and fine grain of Mg-doped BaTiO_3 . Schematic diagram of the profile of acceptor dopants and the grain boundary donor state surface charge for (b) fine grain and (c) coarse grain specimen, respectively. Reproduced with permission from ref. 9. (d) Dielectric permittivity of MLCCs based on fine grained BaTiO_3 varying with temperature. (e) Resistance degradation behavior of fine-grained BaTiO_3 . BT08, BT20, BT30, and BT45 were synthesized using BaTiO_3 powder as a starting material with a size of 80 nm, 200 nm, 300 nm and 450 nm. Reproduced with permission from ref. 59.

Mg-doped BaTiO_3 with the same dopant concentration. The lower conductivity in BaTiO_3 with smaller grain size can be explained by the dopant-rich grain boundary in BaTiO_3 . Fig. 5b and c depict the fine/coarse grain Mg-doped BaTiO_3 with their acceptor dopant (A') and donor-like surface charge (D^*) concentration at the grain/grain boundary, respectively. The donor like surface charge is composed of an excess of interstitial Ti ions, with A-site and oxygen vacancy concentrated at the grain boundary.⁵² Commonly, acceptor dopants tend to be accumulated in the grain boundary region, due to the positive grain boundary surface charge.^{52–55} Thus, when the portion of the grain boundary is large, as acceptors are mainly distributed at grain boundaries, dopant concentration becomes relatively deficient in grains. As shown in Fig. 5b and c, for fine grain samples, the grain itself has lower acceptor dopant concentration than the coarse grain sample, because the fine grain sample has a higher proportion of grain boundary. Acceptors inside the grain are compensated by the generated oxygen vacancy ($[A'] \sim 2[V_O^{**}]$); however, acceptors incorporated in the grain boundary ($[A']_{\text{GB}}$) are mainly charge compensated by donor-like surface charges ($[D^*]$). Therefore, in the grain of fine grain BaTiO_3 , the concentration of oxygen vacancies is lower than that of coarse grain BaTiO_3 . As shown in Fig. 5a, low concentration of V_O^{**} in fine grain BaTiO_3 leads to low ionic conductivity, compared with coarse grain BaTiO_3 . By limiting

the V_O^{**} concentration in BaTiO_3 due to grain size, the resistance degradation behavior of dielectric layers in MLCCs can be improved. The grain size effect on nonlinear dielectric behavior was also reported.⁵⁶ The MLCCs with dielectric layers with larger BaTiO_3 grains show larger dielectric nonlinearity. It is attributed to the degree of tetragonal distortion, intergranular constraints, the density of lattice defects and the range of the domain wall in a high ac field. Therefore, compared to MLCCs with coarse grains, MLCCs with fine grains exhibit high capacitance due to a low nonlinear response.

Furthermore, the grain boundary itself also plays a major role in the insulation resistance of the capacitor. Due to the coordination environment of near Ti^{4+} , V_O^{**} is energetically preferred to be trapped at the grain boundary, confirmed by computational analysis and experimental work.^{57,58} Consequently, when the dielectric layer has fine grains, they have lower oxygen vacancy concentration with larger grain boundaries, resulting in improvement of insulation resistance degradation.⁹ As shown in Fig. 5d and e, Gong and coworkers reported the dielectric properties and resistivity of BaTiO_3 depending on the grain size.⁵⁹ BT08, BT20, BT30, and BT45 were synthesized with BaTiO_3 powder size of 80 nm, 200 nm, 300 nm and 450 nm, respectively. From Fig. 5d, it can be noticed that when the grain size increases, the dielectric permittivity and Curie temperature of the doped BaTiO_3 increase. The electrical resistance of the doped BaTiO_3 increases and the

insulation resistance degradation behavior is improved with decreasing grain size as shown in Fig. 5e. In addition, the time for loss of resistance also increases. The authors also demonstrated the role of the grain boundary in hindering oxygen diffusion through complex impedance studies. They calculated the activation energy for each different grain size based on complex impedance analysis and figured out that the sample with a smaller grain size has a higher activation energy value. This is because the grains of donor and acceptor doped BaTiO₃ have a core–shell structure, which is a chemically heterogeneous microstructure.⁵⁹

4.2. Morphology control of BaTiO₃ raw powder

For developing MLCCs with high capacitance, the dielectric sheet should become thinner. This can be realized by decreasing the particle size of dielectric raw materials.^{3,4,60,61} Moreover, with a fine dielectric powder, the sintering temperature and the failure rate can be lowered to increase the efficiency of the fabrication process. This is because a dielectric layer with fine powder can effectively prevent the electrical short between the Ni inner electrodes due to low surface roughness. Therefore, there have been many reports on the synthesis method for morphology controlled BaTiO₃ for dielectric layers in MLCCs.^{4,60–65} For example, a solvothermal synthesis method of BaTiO₃ nanoparticles in large batches at room temperature was reported (Fig. 6a–d).⁶⁰ By controlling the ratio of solvent mixture and reaction time, the particle size of BaTiO₃ nanoparticles can be varied from 7 nm to 16 nm. The synthesized particles show a narrow size distribution range. With this synthesis method, BaTiO₃ nanoparticles can be easily integrated with functional materials such as low-temperature or reactive materials and substrates. Zhu and coworkers also reported

the hydrothermal synthesis method of BaTiO₃ nanoparticles with different starting materials (Fig. 6e and f).⁶¹ When the authors used barium hydroxide and titanium dioxide as starting materials, two types of BaTiO₃ nanoparticles, coarse-faceted shape and spherical shape, were synthesized. This bimodal size distribution is attributed to the presence of high strain in these nanoparticles due to lattice defects and their compensation by cation vacancies. On the other hand, when barium hydroxide and titanium hydroxide were used as starting materials, spherical BaTiO₃ nanoparticles were obtained with an average grain size of 65 nm and narrow size distribution. From these reports, it can be known that solvent and starting materials are key parameters to synthesize fine BaTiO₃ powder.

The synthesis method of BaTiO₃ nanostructures has also been reported due to their notable advantages such as high surface-to-volume ratio, crystalline quality, and dimensionality.^{64–69} As shown in Fig. 6g, Bao *et al.* reported on the synthesis method of BaTiO₃ nanowires using a simple ion-exchange reaction.⁶⁴ As alkali-metal titanates such as Na₂Ti₃O₇ and K₂Ti₄O₉ have an open layered structure and ion-exchange properties, BaTiO₃ nanowires can be easily obtained by hydrothermal ion-exchange conversion of Na₂Ti₃O₇ nanowires and K₂Ti₄O₉ nanowhiskers. The diameter and length of BaTiO₃ nanowires depend on the dimension of the alkali-metal titanate precursor and both types of BaTiO₃ nanowires are single-crystalline without any impurity phases. Caruntu's group also reported on the controlled synthesis of freestanding, cube-like BaTiO₃ nanocrystals by a soft solution chemical process (Fig. 6h).⁶⁵ When a precursor solution was prepared in an inert atmosphere, the shape of nanocrystals changed from cube-like to cubes with an edge length of 22 nm. The BaTiO₃ nanocubes can be easily

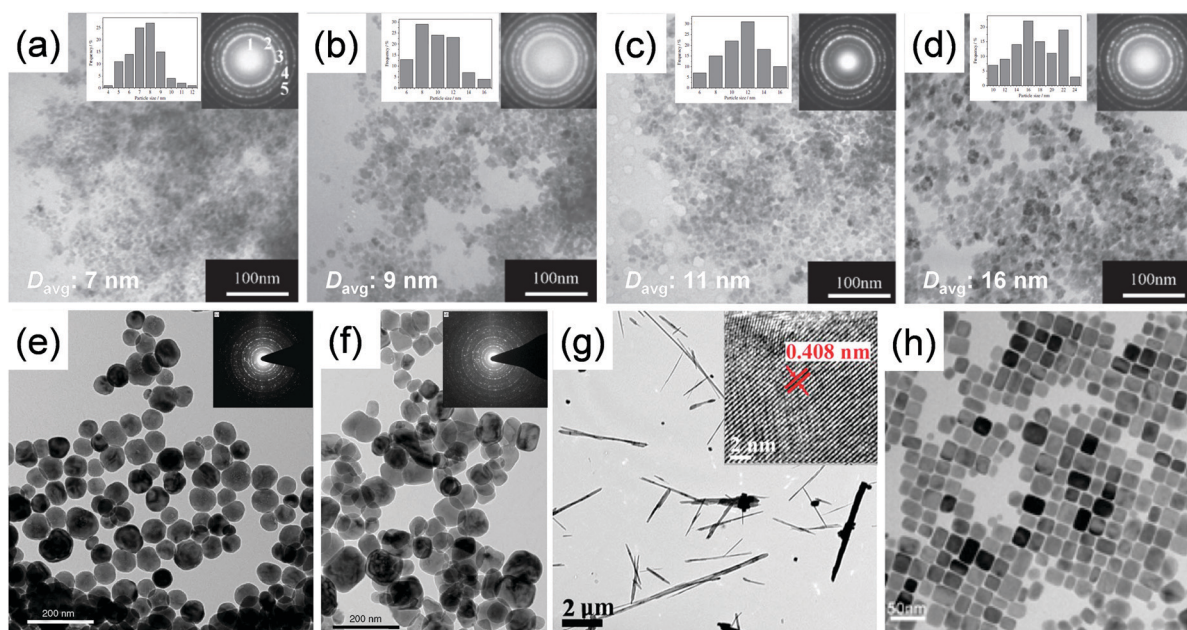


Fig. 6 TEM images and selective area electron diffraction (SAED) patterns of BaTiO₃ nanoparticles and nanostructure. BaTiO₃ nanoparticles prepared with different ethylenediamine/ethanolamine volume ratios of (a) 3 : 0, (b) 2 : 1, (c) 1 : 1 and (d) 1 : 2. Reproduced with permission from ref. 60. BaTiO₃ nanoparticles synthesized with (e) titanium dioxide and (f) titanium hydroxide, respectively. Reproduced with permission from ref. 61. (g) BaTiO₃ nanowires. Reproduced with permission from ref. 64. (h) BaTiO₃ nanocubes. Reproduced with permission from ref. 65.

dispersed in nonpolar solvents, as the BaTiO₃ nanocubes retain oleic acid molecules on their surfaces. Due to excellent stability against aggregation and uniform shape, BaTiO₃ nanocubes can be used as building blocks for the design of dielectric thin films for MLCCs.

4.3. Control of the Ba/Ti ratio and tetragonality in BaTiO₃

The Ba/Ti ratio in BaTiO₃ can affect the dielectric properties of BaTiO₃. This is because the domain wall contribution and tetragonality are significantly changed by the Ba/Ti ratio, which is directly related to the dielectric behavior. As shown in Fig. 7, the dielectric properties of MLCCs based on BaTiO₃ with different Ba/Ti ratios were reported in 2013.⁴⁹ By varying Ba concentration, the ratio of Ba/Ti can be precisely controlled and the MLCCs based on 0.4 mol% (0.4Ba), 1.2 mol% (1.2Ba), 1.6 mol% (1.6Ba) and 2.4 mol% (2.4Ba) Ba-excess BaTiO₃ systems were prepared. Regardless of the Ba concentration, the synthesized BaTiO₃ has a tetragonal structure with the space group of *P4mm* while the tetragonality changes with the Ba concentration. The tetragonality of BaTiO₃ increases with Ba concentration and has the maximum value at 1.6Ba. Above 1.6Ba, it starts to decrease. The authors also controlled the grain sizes of the samples strictly, which are around 260–270 nm, to exclude the grain size effect. In Fig. 7a, the ac field dependence of the dielectric permittivity for 0.4Ba, 1.2Ba, 1.6Ba, and 2.4Ba is presented. The dielectric permittivity of the MLCCs based on the Ba-excess BaTiO₃ system shows an increasing, saturation and decreasing behavior with increasing ac field. When the Ba concentration increases, the dielectric permittivity increases until 1.6Ba, which is the maximum value, and decreases at 2.4Ba. From these results, it can be known that the excess Ba concentration has an impact on the ac field dependence of dielectric properties. For all samples, the threshold field, which is the field value at which the dielectric permittivity starts to be dependent on the AC field, is constant with a value of 0.01 V μm⁻¹. It means that for BaTiO₃ samples with different Ba concentrations, the kind of pinning centers and pinning force which are related to domain wall motion are almost similar. The dielectric permittivity values for 0.4Ba, 1.2Ba, 1.6Ba, and 2.4Ba samples are 2200, 2450, 3100, and 1800 respectively which are larger than the dielectric

permittivity value of 1000, originating from only intrinsic contribution at room temperature. Therefore, the change in the dielectric permittivity value with different Ba concentrations is attributed to the reversible domain wall contribution and density.^{70,71}

Fig. 7b shows the behavior of dielectric permittivity *versus* dc field for 0.4Ba, 1.2Ba, 1.6Ba, and 2.4Ba measured under an ac field of 0.5 V μm⁻¹. As the dc bias increases, the dielectric permittivity decreases and then becomes saturated. The degree of dielectric permittivity variation matches with the dielectric permittivity at the zero dc bias of each sample. In the case of 0.4Ba, 1.2Ba, and 1.6Ba, the dielectric permittivity converges at a dc bias around 3.5 V μm⁻¹ while that of 2.4Ba has a slightly higher value. The variation of dielectric permittivity under dc-bias is mainly due to its nonlinear behavior. Due to high domain wall density or high magnitude of spontaneous polarization, the nonlinearity of dc field dependent dielectric permittivity can be generally alleviated with high dielectric permittivity.^{41,46,72}

Fig. 7c represents the reversible first order reversal curve of doped BaTiO₃ with different Ba concentrations. The reversible distributions have the peak value at the origin, and decrease as α , which is the switching field, moves far from the origin. The value of reversible distribution at zero bias increases as the Ba concentration goes up until 1.6Ba and drops abruptly when Ba concentration becomes 2.4 at%. In the high field region, especially when $\alpha > 3.0$ V μm⁻¹, the distribution of 0.4Ba, 1.2Ba and 1.6Ba converges while 2.4Ba has a larger value. These results are in line with the dc field dependent dielectric properties of the MLCCs based on the Ba-excess BaTiO₃ system. It means that the intrinsic contribution of 2.4Ba is stronger than that of other concentration samples. Therefore, the difference of reversible distributions at the origin is mainly related to the reversible domain wall contributions.⁷⁰ The relationship between the tetragonality of BaTiO₃ and dielectric properties was also reported. By controlling the amount of starting materials, BaCO₃ and TiO₂, the Ba/Ti ratio is determined. When the Ba/Ti ratio is 1, BaTiO₃ shows the highest tetragonality and dielectric permittivity value.^{73,74}

4.4. Doping effects on dielectric properties of BaTiO₃

The origin of the doping process in the dielectric layer starts from the change of electrode metals in MLCCs. At first,

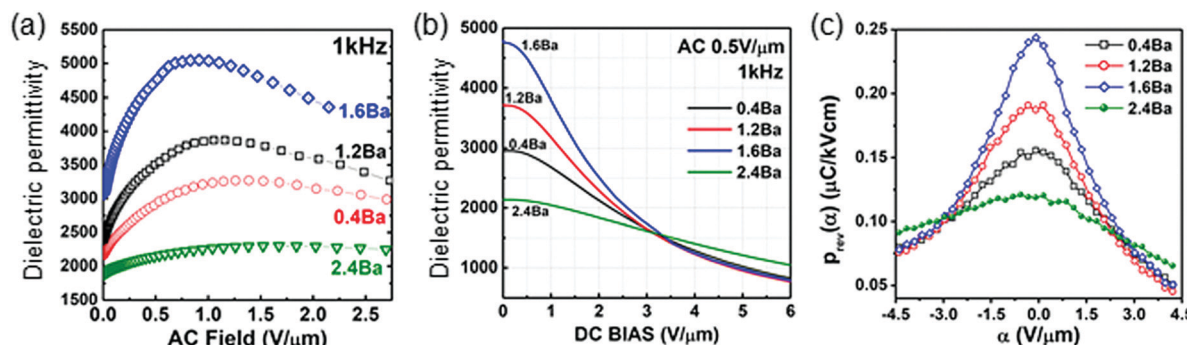


Fig. 7 Dielectric properties of Ba-doped BaTiO₃ based MLCCs. 0.4Ba, 1.2Ba, 1.6Ba and 2.4Ba represent 0.4, 1.2, 1.6 and 2.4 mol% Ba-doped BaTiO₃ based MLCCs. (a) The dielectric permittivity under an ac field. (b) The dc bias characteristics, when they were measured at an ac field of 0.5 V μm⁻¹. (c) The reversible FORC distributions as a function of α , where α is the switching field. Reproduced with permission from ref. 49.

electrodes were mainly composed of noble metals like Pt or Pd which can bear the firing in an oxidative atmosphere. However, with the attention now turned to base metals like Fe, Co, and Ni as electrode materials for they are cheap and abundant, there is a need for a reducing atmosphere to prevent severe oxidation of the metal electrode layer. Although a reducing atmosphere protects metal electrodes from oxidation, it causes the generation of ionized oxygen vacancies in the dielectric layer, especially BaTiO_3 .¹¹ The generated ionic oxygen vacancies give rise to a conduction electron, which leads to high electronic conductivity of the dielectric layer. For the nonreducible BaTiO_3 dielectrics, three key factors, Ba/Ti ratio, oxygen partial pressure, and doping, are commonly considered. Among these factors, doping is the most efficient process implemented in the BaTiO_3 layer in MLCCs.^{75–78} When dopants, especially acceptors, are introduced, they form the point defect which traps the electron tightly. Therefore, doping can help in the preparation of highly insulating dielectric materials in a reducing environment.

Various dopants were introduced into BaTiO_3 and their influence on the dielectric properties of BaTiO_3 was intensively investigated by numerous researchers.^{79–83} According to the dopants' oxidation state and site occupancy, the dielectric properties of BaTiO_3 can be significantly changed and controlled. Fig. 8a illustrates the unit cell of perovskite BaTiO_3 . Dopant atoms can be introduced into the A site (barium atom site) and B site (titanium atom site) which depends on other variables such as ionic radius of dopants or the synthesis condition. In most cases, BaTiO_3 can be doped through the standard solid state reaction and hydrothermal reaction.^{84–86}

Many rare earth elements are applied as dopants to enhance the dielectric properties and due to their amphoteric behavior, the influence of their site occupancy on dielectric properties has been studied intensively.^{87–89} Which site is occupied is mainly determined by the effective radius of rare earth elements. Fig. 8b shows the effective ionic radius of rare earth elements that show the amphoteric behavior. These rare earth elements have an intermediate effective ionic radius between that of Ba and Ti.⁹⁰ Among them, Dy is the most commonly used for doping because Dy is extremely cheap when compared to other rare earth elements as illustrated in Fig. 8c. Also unlike Eu, which has 2+ and 3+ valence states, which can be detrimental to the dielectric properties, Dy has a fixed valence state of 3+. Rare earth elements with a fixed valence state of 3+ can act as a donor for A site doping and acceptor for B site doping. When rare earth elements are doped as a donor at the A site, a decrease of the Curie temperature and an increase of the dielectric permittivity value were reported. For example, Mizuno *et al.* demonstrated a decrease of the Curie temperature when the concentration of Eu ions at the A site increases.⁹¹ The drop of the Curie temperature has been also found in Y-doped BaTiO_3 , Gd-doped BaTiO_3 , and Y-doped BaTiO_3 .⁹²

The rare earth dopants can also have an influence on the formation of the grains of BaTiO_3 which leads to changes in dielectric properties.^{93–96} Fig. 8d shows the temperature dependency of the dielectric permittivity measured from MLCCs based on the Ho and Dy co-doped BaTiO_3 system. The MLCC based on BaTiO_3 doped with equal contents of Dy and Ho shows the lowest dielectric permittivity and TCC. It can be

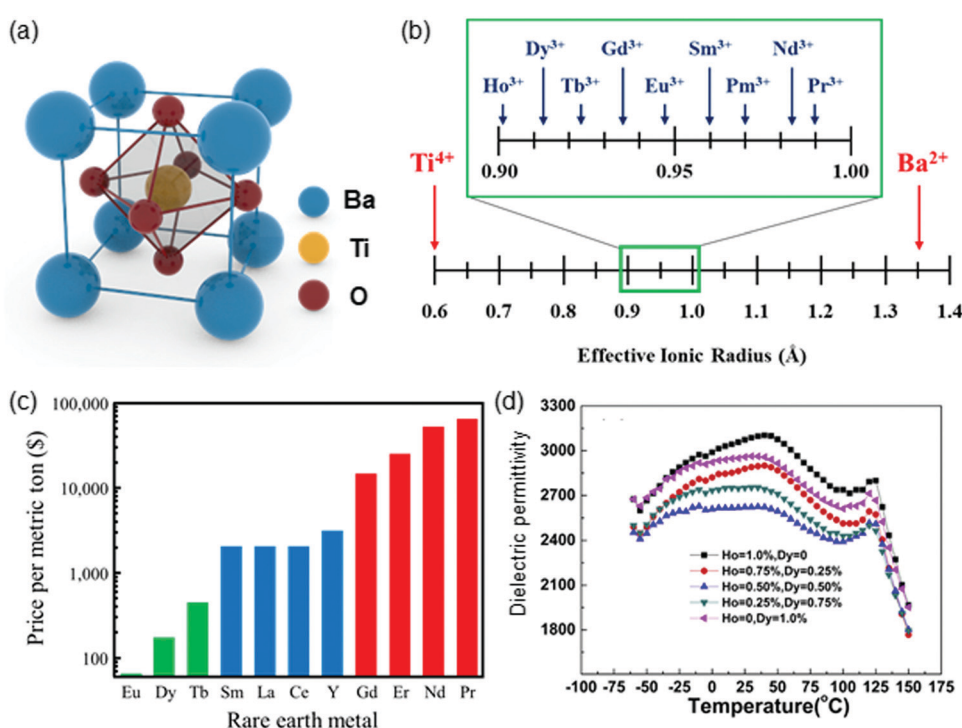


Fig. 8 (a) Schematic of the crystal structure of BaTiO_3 . (b) Effective ionic radius of various rare earth elements. (c) Average prices of rare earth metals. (d) Doping effect on the temperature dependent dielectric permittivity of BaTiO_3 . Reproduced with permission from ref. 93.

explained by the grain size difference of BaTiO_3 doped with different compositions of Ho and Dy. The grain sizes for ($\text{Ho} = 1.0\%$, $\text{Dy} = 0.0\%$), ($\text{Ho} = 0.75\%$, $\text{Dy} = 0.25\%$), ($\text{Ho} = 0.5\%$, $\text{Dy} = 0.5\%$), ($\text{Ho} = 0.25\%$, $\text{Dy} = 0.75\%$) and ($\text{Ho} = 0.0\%$, $\text{Dy} = 1.0\%$) were 265.2, 240.2, 223.2, 234.4, and 243.5 nm respectively. Considering that the dielectric permittivity increases with the grain size until the grain size is 1 μm , the trend in dielectric permittivity matches well with the grain size. The shrinkage of the grain size when two different rare earth elements are co-doped is supposed to be influenced by the interaction of dopants. The inhibition of grain growth by the addition of rare earth elements was also reported by several groups.^{94–97} While the mechanism for the behavior of rare earth dopants is still not clear, Kim *et al.* proposed that the extraction of Ti^{4+} at the grain boundary owing to introducing the dopants results in the formation of a eutectic phase, which affects the grain growth.⁹⁸

Alkali metal and transition metal elements are dopants that are most intensively studied. In most cases, alkali/transition metal elements are mainly introduced into the B site of BaTiO_3 where they create a trap site for electrons and act as acceptors.⁸⁴ When they are introduced into BaTiO_3 , BaTiO_3 becomes insulating in nature. Besides the change of the electronic structure, doping can also directly affect the microstructure of BaTiO_3 . Gong *et al.* reported the dielectric permittivity of Mn-doped BaTiO_3 in the temperature range of $-75\text{ }^\circ\text{C}$ to $150\text{ }^\circ\text{C}$ as shown in Fig. 9a.⁸⁴ The dielectric permittivity value increases with Mn concentration until 0.5 mol%. When the Mn concentration reaches 1.0 mol%, the dielectric permittivity becomes similar

to that of pure BaTiO_3 . The increment of dielectric permittivity with Mn doping is related to the variation of grain size. When Mn is introduced into BaTiO_3 , it is accumulated in the outer region of the grains, forming the core–shell shaped structure and restricts the grain growth.^{99,100} However, if the concentration of Mn is larger than 0.5 mol%, the Mn element becomes enriched at the grain boundaries and blocks the diffusion of other atoms during grain growth; therefore, it hinders the densification of the dielectric layer and leads to a reduction of dielectric permittivity despite the smaller grain size of BaTiO_3 .

Some elements, such as Ni and Ca, can also be placed at the A site. Pb or Bi doping is implemented to extend the working range of MLCCs with BaTiO_3 dielectric layers by elevating the Curie temperature. However, Ca is now extensively used as a substitute rather than Pb or Bi due to the environmental problem. Zhang *et al.* reported temperature dependent dielectric properties of BaTiO_3 depending on the doping of Ca at the Ba and Ti site.¹⁰¹ The authors synthesized $\text{Ba}_{1-x}\text{Ca}_x\text{TiO}_3$ and $\text{BaTi}_{1-x}\text{Ca}_x\text{O}_3$ using the semiwet route and the mixed oxide route, respectively. From the lattice parameters measured by XRD analysis, they confirmed the stoichiometry of $\text{Ba}_{1-x}\text{Ca}_x\text{TiO}_3$ and $\text{BaTi}_{1-x}\text{Ca}_x\text{O}_3$. Fig. 9b shows Curie temperature dependency on the dopant concentration of $\text{Ba}_{1-x}\text{Ca}_x\text{TiO}_3$ and $\text{BaTi}_{1-x}\text{Ca}_x\text{O}_3$. The Curie temperature of $\text{Ba}_{1-x}\text{Ca}_x\text{TiO}_3$ increases as the concentration of Ca reaches $x \sim 0.08$.^{101,102} In contrast to A-site occupancy by Ca dopants, a marked decrease of the Curie temperature was observed when Ca is placed at the B site.^{83,103} The shift of Ca to the B site can be seen in the BaO excess

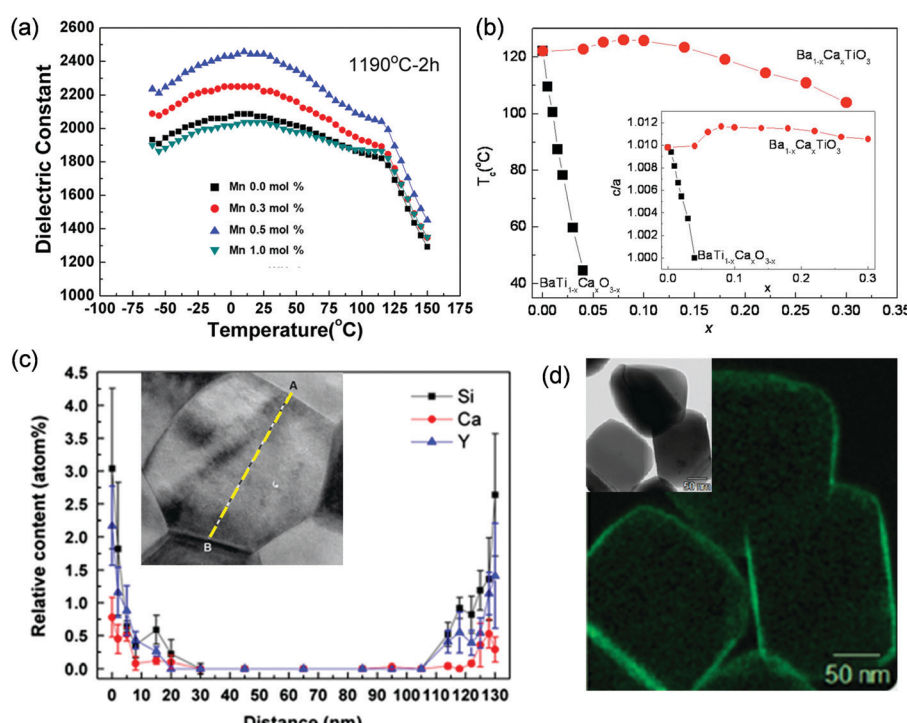


Fig. 9 (a) The dielectric permittivity of Mn-doped BaTiO_3 as a function of temperature. Reproduced with permission from ref. 84. (b) T_C vs. x for $\text{Ba}_{1-x}\text{Ca}_x\text{TiO}_3$ and $\text{BaTi}_{1-x}\text{Ca}_x\text{O}_3$. Reproduced with permission from ref. 101. (c) TEM EDS line profile and (d) EDS mapping image of the core–shell structure of doped BaTiO_3 ceramics and nanopowder, respectively. Reproduced with permission from ref. 55 and 110.

environment during the synthesis.^{11,104} Similar to Ca, Ni can also be doped into both A and B sites of BaTiO₃. It is reported that the oxygen vacancy concentration is higher in the B site Ni-doped BaTiO₃ rather than in the A site Ni-doped BaTiO₃.^{105,106} This leads to the emergence of hexagonal BaTiO₃, which is stabilized by oxygen vacancy, only in B site Ni-doped BaTiO₃. Other transition metal dopants, such as Fe, Co, and Cr, can also stabilize the hexagonal phase of BaTiO₃.^{107–109}

In many cases, when the dopants are introduced, it is reported that dopants are accumulated in the grain boundary to form a core-shell structure. Fig. 9c shows the line profile of the dopant elements in Y and Ca-co-doped BaTiO₃.⁵⁵ Transmission electron microscopy (TEM) and energy dispersive spectroscopy (EDS) analyses are implemented to check the distribution of dopants in a single grain. According to the line profile, dopants are mainly accumulated in the grain boundary region, similar to the case of the Mn-doped BaTiO₃ core-shell structure.⁸⁴ The synthesis of raw materials for dielectric layers, which have a core-shell structure, was also reported.¹¹⁰ The core-shell structure can be easily distinguished using EDS mapping, as shown in Fig. 9d. It can be seen that the Gd elements are mainly distributed in the outer region of the grain.

4.5. Wide temperature range stability

As the usage of MLCCs has become broader, the environment in which MLCCs have to be operated is now harsher than ever. They are applied in areas such as an automobile engine and rockets for outer space and these applications require MLCCs to work under conditions with a broad temperature range.^{95,96} Till recently, X7R (Temperature Coefficient of Capacitance, TCC $\leq \pm 15\%$ from -55 to 125 °C), X8R (TCC $\leq \pm 15\%$ from -55 to 150 °C) and X9M (TCC $\leq \pm 50\%$ from -55 to 200 °C) MLCCs were commercialized. While the X7R MLCC is a BaTiO₃-based system, the X8R MLCC applies the Ca-doped BaTiO₃ system because of the high Curie temperature and nonlinearity achieved by Ca doping. Therefore, the TCC of the X8R MLCC is advantageous for high temperature applications above 125 °C.¹¹¹ For the X9M MLCC, it is also based on the Ca-doped BaTiO₃ system, but the warranted TCC is $\pm 50\%$ due to the limitation in the Curie temperature. Recently, higher standards of operation temperature and reliability are required than that of the conventional MLCCs, like the X9R standard (TCC $\leq \pm 15\%$ from -55 to 200 °C). The commercialized X9R MLCCs are based on the CaZrO₃ system, but their capacitance is very low due to paraelectric properties of CaZrO₃. For high capacitance X9R MLCCs, Bi-based perovskite systems have been studied.^{112–124} However, precious inner electrode materials, such as Pt and Pd, are needed owing to severe volatilization of Bi during sintering in a reducing atmosphere. In order to meet these higher requirements, the composites of BaTiO₃ and Bi-based perovskites have been extensively investigated for higher thermal reliability and high Curie temperature.^{125–131} In addition, to utilize the maximum dielectric permittivity near room temperature, the methods to shift the Curie temperature to room temperature without dielectric permittivity loss have been also studied.^{100,132,133}

The temperature dependency of BaTiO₃ can be briefly explained with the behavior of the micro-domains, which are affected by the forces applied on the BaTiO₃ grain.¹³⁴ Fig. 10a represents the temperature dependency of the permittivity of doped BaTiO₃ with the scheme of micro-domain motion in the different temperature range. In the low temperature range, the permittivity increases with the temperature. Then, it reaches the maximum value and decreases after the temperature of the maximum permittivity, which is the Curie temperature. The temperature dependence of dielectric properties is deeply related to the forces on the BaTiO₃ grain, which are the interaction between the polarized microdomains (F_i), the thermal vibration force (F_v) and the external electric field force (F_e). First, polarized micro-domains are large enough because F_v can be ignored due to low temperature and F_i is larger than F_e near the freezing temperature of transition (T_f), resulting in the random distribution of dipoles. Over the T_f , as the polarized micro-domains decrease, F_e becomes dominant due to the decrease of F_i . Thus, dipoles start to align and dielectric permittivity increases. When the temperature reaches the Curie temperature, the alignment of dipoles becomes maximum and dielectric permittivity has the highest value. Above the Curie temperature, F_v starts to be dominant and F_i now becomes insignificant. Due to the stronger thermal vibration, micro-domains can easily vibrate in equivalent directions and this suppresses the macroscopic polarization. A further increase of the temperature over the burns temperature (T_b) results in complete vanishment of local polarization.¹³⁴ Ben *et al.* reported the shift of the Curie temperature of BaTiO₃ due to Gd and La doping.¹³² Fig. 10b shows the variation of dielectric permittivity with temperature of Gd-doped BaTiO₃ and La-doped BaTiO₃. The Curie temperature of Ba_{1-x}Gd_xTi_{1-x/4}O₃ and Ba_{1-x}La_xTi_{1-x/4}O₃ varying with doping concentration is summarized in Table 2.

For both dopants, the peak of the dielectric permittivity is still observed, which indicates the Curie temperature. When the dopants are introduced in the concentration of 0.05 and 0.04, respectively, for Ba_{1-x}Gd_xTi_{1-x/4}O₃ and Ba_{1-x}La_xTi_{1-x/4}O₃, the decrease of the Curie temperature occurred. The rate of Curie temperature decrease with dopant concentration differs for Gd and La, as shown in the inset of Fig. 10b. It is well known that dopants which induce the removal of Ti ions or oxygen ions for the charge balance disrupt the ferroelectric domain in BaTiO₃ severely.^{135–137} Therefore, they result in steep suppression of the Curie temperature with the rates of more than 10–20 °C per at%.^{101,133} For Gd and La, their Curie temperature change is mainly caused by the generation of the Ti vacancy due to the A site doping. While La-doped BaTiO₃ has a Curie temperature variation rate of 24 °C per at%, Gd shows 8 °C per at% which is far from the rates commonly induced by Ti vacancy generation. This phenomenon can be rationalized by the difference in the degree of the strain applied on BaTiO₃ due to size mismatch. Gd has a much smaller ionic radius for 12-fold coordination when compared to that of La. Therefore, larger size difference with Ba and Gd leads to more strain on Gd-doped BaTiO₃. As a result, this strain cancels out the

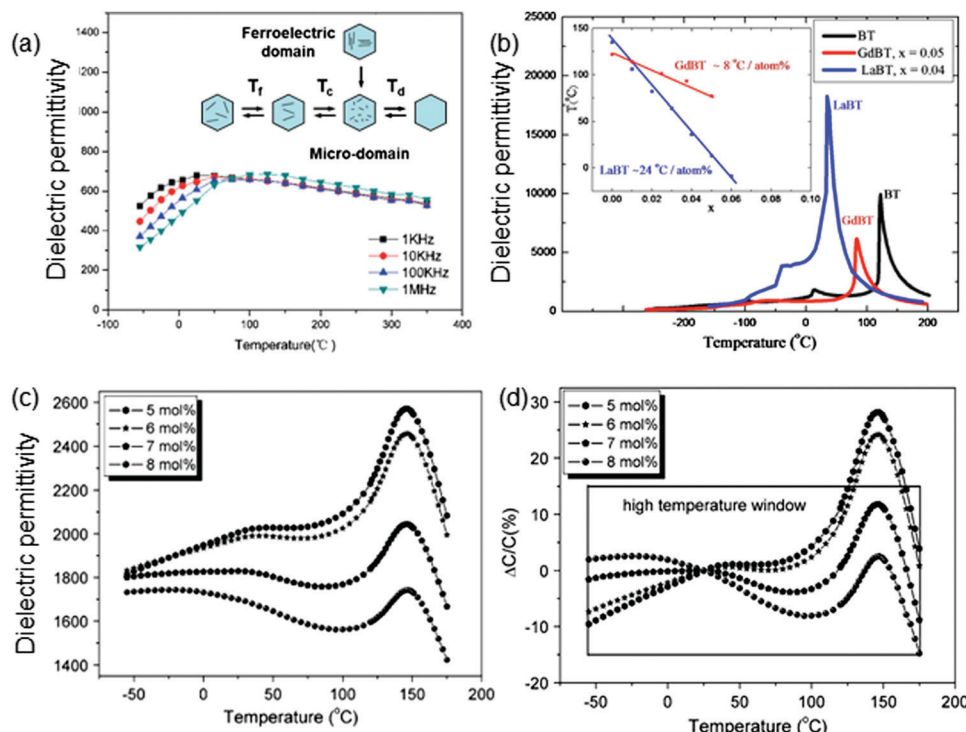


Fig. 10 (a) The temperature dependence of dielectric permittivity for the Bi^{3+} , Na^+ , Zn^{2+} , Nb^{5+} doped BaTiO_3 dielectric system under various ac fields. Reproduced with permission from ref. 134. (b) Dielectric permittivity at 100 kHz vs. temperature for undoped BaTiO_3 , $\text{Ba}_{0.95}\text{Gd}_{0.05}\text{Ti}_{0.9875}\text{O}_3$ and $\text{Ba}_{0.95}\text{La}_{0.04}\text{Ti}_{0.99}\text{O}_3$ ceramics. Reproduced with permission from ref. 132. Temperature dependence of the (c) dielectric permittivity and (d) capacitance change of BaTiO_3 doped with various CaZrO_3 contents. Reproduced with permission from ref. 127.

Table 2 Curie temperature of $\text{Ba}_{1-x}\text{Gd}_x\text{Ti}_{1-x/4}\text{O}_3$ and $\text{Ba}_{1-x}\text{La}_x\text{Ti}_{1-x/4}\text{O}_3$ varying with doping concentration¹³²

Curie temperature (°C)			
<i>x</i>	$\text{Ba}_{1-x}\text{Gd}_x\text{Ti}_{1-x/4}\text{O}_3$	<i>X</i>	$\text{Ba}_{1-x}\text{La}_x\text{Ti}_{1-x/4}\text{O}_3$
0.00	135.53	0.00	121.59
0.01	106.39	0.01	113.72
0.02	82.25	0.025	100.84
0.03	64.10	0.0375	92.62
0.04	36.12	0.05	76.53
0.05	12.96		
0.06	-9.30		

detrimental effect on the Curie temperature, which is caused by the Ti vacancies.¹³²

The temperature dependence of dielectric nonlinearity can be alleviated by a complete solid solution with BaTiO_3 and CaZrO_3 .¹²⁷ Fig. 10c and d show the dielectric permittivity and capacitance change of BaTiO_3 doped with CaZrO_3 of varying concentration under different temperatures. By increasing the concentration of CaZrO_3 , the dielectric permittivity change near the Curie temperature is lowered. The gradual and broad peak in the range from -50 °C to 100 °C is mainly attributed to the ferroelectric-paraelectric phase transition of the outer region, in which dopants are mainly distributed. With the addition of 7 and 8 mol% CaZrO_3 , the capacitance change is less than 15% in the range of -55 to 175 °C, which satisfies the EIA standard of X8R.

Lee and coworkers also reported that the temperature dependent capacitance change can be suppressed by introducing a constraining layer.¹²⁶ The constraining layers generate internal stress to the dielectric layer during the sintering process and affect the densification rate of BaTiO_3 , resulting in grain size reduction. Although the dielectric permittivity value at the Curie temperature decreases, improved thermal stability is observed. The high performance and temperature-stable MLCCs can be also obtained by using the BaTiO_3 -based dielectric layer with a hierarchical structure.¹²⁵ By combining $(\text{Ba}, \text{Bi})\text{TiO}_3$ and $\text{Ba}(\text{Ti}, \text{Zr})\text{O}_3$, the MLCCs show a better dielectric permittivity value and lower temperature capacitance changes, when compared to MLCCs based on the pure BaTiO_3 system.

4.6. DC-bias characteristics: capacitance variation under dc-bias

The capacitance aging under dc bias rises up as the critical issue for developing high performance MLCCs, as the thickness of the dielectric layer becomes thinner. This is because the strength of the electric field applied on the dielectric layer increases. When the dielectric layer is exposed to such a harsh condition, it commonly loses the capacitance. The mechanism of capacitance aging under a dc electric field is illustrated in Fig. 11a. Without dc bias, the dipoles in each grain are arranged randomly. However, when dc bias is applied, the dipoles start to align in the direction of applied dc bias and they line up in a single direction. Thus, under high external dc bias, internal

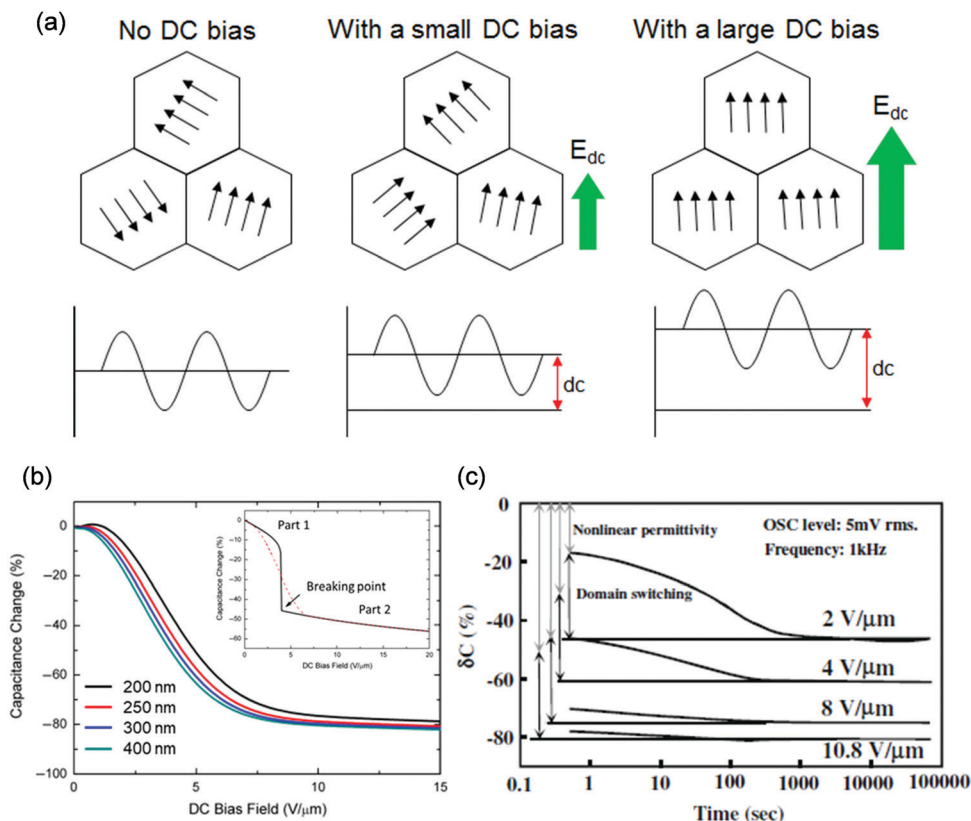


Fig. 11 (a) Schematic illustrations for capacitance aging under dc bias. (b) Capacitance change of BaTiO₃ with various grain sizes. Reproduced with permission from ref. 138. (c) Capacitance aging curves of MLCCs based on a 0.8 mol% Mn-doped BaTiO₃ system at 110 °C measured under different DC fields. Reproduced with permission from ref. 140.

dipoles are fixed in the direction of applied bias. It lowers the rate of polarization change by the AC field, leading to a decrease of dielectric permittivity. Commonly, when the grain size becomes smaller or dielectric permittivity decreases, the change of capacitance due to dc bias decreases.

Sun *et al.* demonstrated the grain size effect on dielectric response under dc bias based on a theoretical model, as shown in Fig. 11b.¹³⁸ The authors calculated the threshold external dc bias for the abrupt capacitance change of MLCCs. The MLCCs with finer grains exhibit higher threshold voltage due to the motion of domain walls. They also compared the experimental and theoretical results. The MLCCs show a gradual drop of capacitance change with increasing dc bias and a saturated value, not the abrupt change shown in calculated results. This is because the grains in MLCCs are not uniform which will lead to different physical properties. Therefore, for each grain, the threshold value for external bias varies. The tetragonality of BaTiO₃ can also make an impact on the dc-bias characteristics of MLCCs.¹³⁹ The dielectric permittivity of BaTiO₃ is significantly decreased when the tetragonality increases. It contributes to the larger capacitance change. This is mainly due to the increased anisotropy in the dielectric permittivity, resulting in a smaller dielectric permittivity along the *c*-axis direction.

Tsurumi and coworkers reported the capacitance aging of MLCCs based on the Ho, Mg, and Mn-doped BaTiO₃ system

under dc bias and its mechanism.¹⁴⁰ Fig. 11c shows the capacitance aging curve of the MLCCs under different dc bias. The capacitance change is divided into two components, nonlinear permittivity and domain switching. This result is in good agreement with the previous study.¹⁴¹ The first stage is a sudden drop of capacitance due to the nonlinear permittivity of the dielectric, and the second stage is a gradual capacitance change originating from the switching of 90-degree domains in the core of BaTiO₃. This behavior can be fully understood from the mechanism of domain wall motion in doped BaTiO₃. Before aging, in BaTiO₃, there are domain walls, which are mostly clamped by defect dipoles resulting from negatively charged Mn sites and positively charged oxygen vacancies. When the dc bias is first applied, the effect of domain switching is negligible, as a small number of unclamped domain walls move. Over time, the continuous application of the dc field moves the electrons of the negatively charged Mn sites. Because Mn is multivalent it can exist as an Mn⁴⁺ state without having any charges in the Ti site and the electrons from Mn sites eliminate positively charged defect dipoles. This enhances the motion of domain walls to align in the direction of the *c*-axis. Finally, the domains in BaTiO₃ are fully aligned and the change of capacitance is saturated. With increasing dc field, the time for capacitance change saturation is reduced and the portion

of the second stage is depressed, as clamped domain walls move regardless of the pinning centers. From this phenomenon, it is possible to understand the severe aging of doped BaTiO₃ under higher field due to the scaling of MLCCs.

4.7. Frequency dependence of dielectric properties

For dielectric materials, such as BaTiO₃, it is well known that dielectric permittivity has frequency dependency due to interfacial/space charge polarization, oriental/dipolar polarization, ionic polarization, and electronic polarization. Each polarization mechanism occurs due to the accumulation of charge at the interface, the alignment of the dipole, oscillation of the ions and shift of the electron cloud, respectively. For the polarization phenomena, sufficient time is required depending on their polarization mechanisms. When the field changes too rapidly, polarization cannot follow the field and dielectric loss occurs. For these polarization mechanisms, dielectric loss occurs at their own distinct frequency range. This is because the variation of dielectric permittivity owing to polarization is directly related to impurity, defect and space charge carrier transport processes in the dielectric material. Therefore, the frequency dependent dielectric properties of BaTiO₃ have been extensively studied.^{13,142,143}

The frequency dependent dielectric properties of Mg-doped BaTiO₃ were reported in 2011.¹⁴⁴ Fig. 12a and b show the dielectric permittivity of Mg-doped BaTiO₃ with coarse grains and fine grains as a function of frequency. For both coarse and fine grain specimens, a steep increase of the dielectric permittivity along with frequency decrease is observed under a frequency of 1 Hz. This behavior is mainly caused by the charge species accumulated at the interface of electrode and dielectric material, which is also called stoichiometric polarization.^{145,146} On the other hand, dielectric relaxation occurs over the frequency of 10 Hz only in the coarse specimen. The dielectric relaxation in this range results from the space charge polarization at grain boundaries due to conducting charge carriers. For Mg-doped BaTiO₃ with fine grains, the thickness of the depletion layer of the grain boundary becomes comparable to the grain size.^{9,147} Thus, it leads to an extremely limited portion of the conducting region in the grain and suppresses the space charge polarization at the grain boundary.

The frequency-dependent dielectric properties can be controlled by the formation of composites with BaTiO₃ and ferromagnetic materials.¹⁴⁸ Fig. 12c represents the frequency dependence of dielectric permittivity measured from (100 – x)BaTiO₃/xLa_{0.7}Ca_{0.3}MnO₃ composites. As the portion of La_{0.7}Ca_{0.3}MnO₃ (LCMO) increases, dielectric permittivity increases, which means that the polarization is strengthened. Considering that the frequency range is around 10²–10⁴ Hz, interfacial and space charge polarization occur in the composites. As mentioned before, for the interfacial and space charge polarization charge carriers have to move and be piled up at the interfaces. In the composites, there are two conduction channels for the charge carriers, the direct contact between BaTiO₃ grains and embedded LMCO grains which are much more conducting when compared to insulating BaTiO₃. With the increase of the LMCO amount, grains of composites become more conducting. It means that charge carriers can easily move to interfaces. Thus, the accumulation of the charge carriers at interfaces requires less time, resulting in the enhancement of the polarization and decrease of the dielectric loss at the high frequency region.

In addition to the influence of space charge polarization, Tsurumi *et al.* reported ionic and dipolar polarization in BaTiO₃ based materials.¹⁴⁹ For BaTiO₃ and Zr-doped BaTiO₃, the dielectric relaxation in the MHz to GHz region is attributed to the dielectric domain wall contribution and polar nanoregion in relaxor materials, respectively. On the other hand, ionic polarization mainly contributes to the dielectric relaxation of Sr-doped BaTiO₃. The relaxation frequency near the THz region of Sr-doped BaTiO₃ is appropriate for high-frequency applications.

4.8. Insulation resistance degradation

Generally, in order to evaluate the reliability of MLCCs, a highly accelerated lifetime test (HALT) is performed to predict the lifetime of the MLCCs based on the Eyring equation. As shown in Fig. 13a, MLCCs show an increase in leakage current and an electrical breakdown under a dc electric field. These are attributed to insulation resistance (IR) degradation behavior and result in the long-term failure of MLCCs.¹⁵⁰ The IR degradation behavior of MLCCs can be explained by the electromigration of oxygen vacancies ($V_O^{••}$) in BaTiO₃ dielectric layers (Fig. 13b–d).

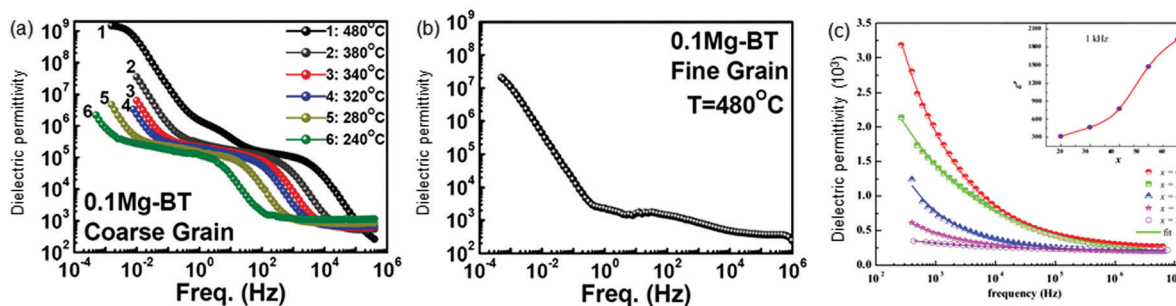


Fig. 12 Dielectric permittivity as a function of frequency for 0.1 mol% Mg-doped BaTiO₃ ceramics with (a) coarse grains and (b) fine grains, respectively. Reproduced with permission from ref. 144. (c) Frequency dependence of the dielectric permittivity of (100 – x)BTO/(x)LCMO composites with x = 20, 30, 40, 50 and 60 wt%. Reproduced with permission from ref. 148.

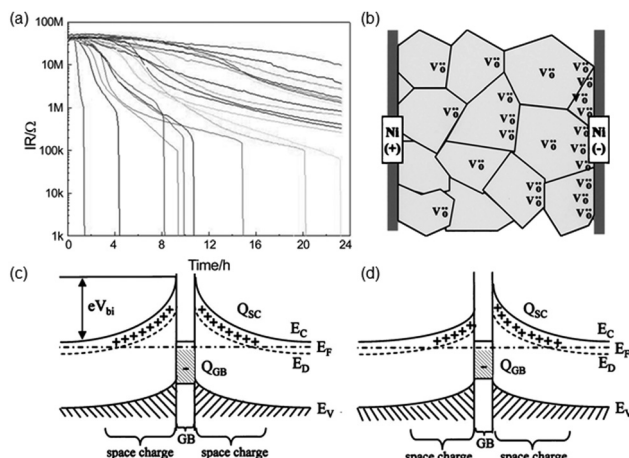


Fig. 13 (a) IR degradation behavior of BaTiO_3 based MLCCs. Reproduced with permission from ref. 150. (b) Schematic illustration of oxygen vacancy concentration in the degraded MLCC. Schematic diagram for changes in the Schottky barrier height eV_{bi} as a function of acceptor charge density at the grain boundaries for the (c) pristine capacitor and (d) degraded capacitor. Reproduced with permission from ref. 154.

As MLCCs are sintered in a reducing atmosphere to avoid oxidation of nickel inner electrodes, a large number of $\text{V}_\text{O}^{\bullet\bullet}$ can be formed in the BaTiO_3 layer. It means that the dielectrics of MLCCs are based on the acceptor-doped BaTiO_3 system as a point of defect chemistry.^{9,151,152} For the as-produced MLCCs, adequate IR characteristics can be observed. Because $\text{V}_\text{O}^{\bullet\bullet}$ are randomly distributed in the dielectric layer, the symmetric Schottky barrier is formed across the grain boundary (Fig. 13c).^{153,154} When MLCCs are subjected to a dc applied bias, the electromigration of $\text{V}_\text{O}^{\bullet\bullet}$ occurs, resulting in depletion and pile-up of $\text{V}_\text{O}^{\bullet\bullet}$ in the anodic region and cathodic region, respectively. The interfacial region and grain boundary near the cathode become n-type and the asymmetric Schottky junction is formed across the dielectric layers like the situation of the forward-biased p-n junction (Fig. 13d). Hence, the leakage current is enhanced during the degradation, resulting in IR degradation and device breakdown. Recently, the electric field across dielectric layers, which affect the migration of $\text{V}_\text{O}^{\bullet\bullet}$, has become higher, as the dielectric layers have become thinner for the high capacity of MLCCs. Therefore, new physical models and approaches to explain and predict the accurate lifetime of MLCCs have been proposed by several groups.^{155,156} However, the suppression of IR degradation in BaTiO_3 and understanding its mechanism are still key issues for developing MLCCs with high performance and reliability.

It is well known that MLCCs with dielectric layers consisting of small grain size show improvement in the lifetime, as the grain boundary interrupts the $\text{V}_\text{O}^{\bullet\bullet}$ transport.^{9,153,154,157,158} However, the grain size control is not an effective solution because it only reduces transport. When BaTiO_3 is doped with acceptors, the number of $\text{V}_\text{O}^{\bullet\bullet}$ can be fixed through ionic compensation. It results in the suppression of the electron generation and improvement of IR. Therefore, many researchers have intensively studied the doping effects on the IR degradation behavior of BaTiO_3 .^{3,15,151,159–164} The valence state of the dopants can

affect the IR degradation behavior of BaTiO_3 .^{165–168} For example, Randall's group reported the IR degradation behavior of fixed valence acceptor (Mg) and variable valence acceptor (Mn)-doped BaTiO_3 based MLCCs.¹⁶⁸ As shown in Fig. 14a, Mg-doped BaTiO_3 shows more severe resistance degradation and a shorter time for breakdown, increasing with Mg doping concentration. This is because the bulk grain conductivity and the portion of ionic conduction contribution increase as the Mg doping concentration increases.^{151,163,164} On the other hand, Mn-doped BaTiO_3 shows less IR degradation behavior, as Mn doping concentration increases (Fig. 14b). These results are attributed to multi-valence state Mn. After electromigration of $\text{V}_\text{O}^{\bullet\bullet}$ under an electric field, electron generation in the cathodic region by accumulation of $\text{V}_\text{O}^{\bullet\bullet}$ and hole generation in the anodic region by the depletion of $\text{V}_\text{O}^{\bullet\bullet}$ can be inhibited by the valence change ($\text{Mn}^{2+} \rightarrow \text{Mn}^{3+} \rightarrow \text{Mn}^{4+}$ in the anodic region and $\text{Mn}^{4+} \rightarrow \text{Mn}^{3+} \rightarrow \text{Mn}^{2+}$ in the cathodic region).^{169–171} In addition, a strong defect association such as $\text{Mn}_{\text{Ti}}^{\text{II}} - \text{V}_\text{O}^{\bullet\bullet}$, which can be generated in Mn-doped BaTiO_3 , can suppress electromigration of $\text{V}_\text{O}^{\bullet\bullet}$ effectively.¹⁷² Using impedance analysis and a defect chemical model, the authors demonstrate that the concentration of $\text{V}_\text{O}^{\bullet\bullet}$ in Mn-doped BaTiO_3 is significantly decreased during the cooling process. It indicates that the increase of the concentration of $\text{V}_\text{O}^{\bullet\bullet}$ is negligible, regardless of the increase in Mn doping concentration. Therefore, variable acceptor-doped BaTiO_3 shows more stable and excellent IR characteristics due to the lower concentration of $\text{V}_\text{O}^{\bullet\bullet}$ and the high electron/hole trapping effect originating from the multivalence nature of Mn. As shown in Fig. 14c and d, the IR degradation behavior of Mg-doped BaTiO_3 and Mn-doped BaTiO_3 after reoxidation annealing treatment in a N_2 atmosphere was also investigated. Generally, the IR degradation behavior of BaTiO_3 can be improved after annealing treatment in an oxidizing atmosphere because it can decrease $\text{V}_\text{O}^{\bullet\bullet}$ concentration effectively. The Mg-doped BaTiO_3 specimens show similar IR

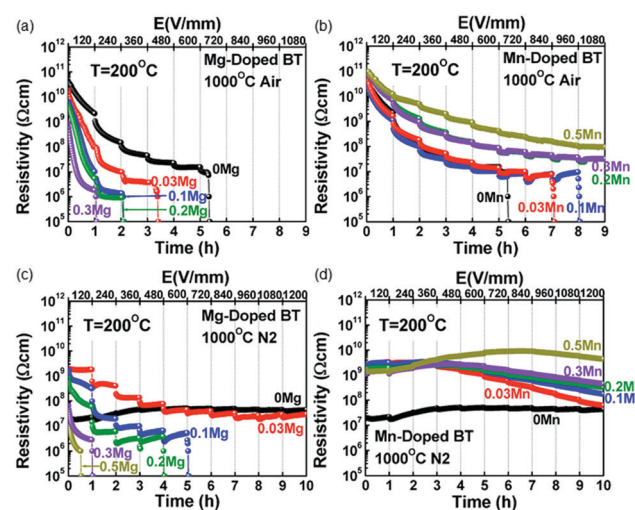


Fig. 14 IR degradation behavior of (a) Mg and (b) Mn-doped BaTiO_3 ceramics, reoxidation annealed at 1000 °C in an air atmosphere, and (c) Mg and (d) Mn-doped BaTiO_3 ceramics, reoxidation annealed in a N_2 atmosphere. Reproduced with permission from ref. 168.

degradation behavior and lower resistivity values due to a slight reduction, compared with that annealed in the air for reoxidation. However, for Mn-doped BaTiO_3 , more stable and improved IR degradation behavior is observed, compared with that of Mn-doped BaTiO_3 annealed in air. This is because the ratio of neutral or hole trapped acceptor and ionized acceptor in BaTiO_3 , which can trap electrons and holes, respectively, becomes similar when acceptor doped BaTiO_3 is annealed in a slightly reducing atmosphere. For the improved IR of BaTiO_3 , variable valence acceptor dopants are more attractive than fixed valence acceptor dopants because nonreducibility can be obtained without the formation of a considerable amount of $\text{V}_\text{O}^{\bullet\bullet}$.

The IR degradation behavior of BaTiO_3 can also be affected by the site occupancy of the dopants.¹⁷³ For example, the substitution of Ca for Ba in BaTiO_3 causes the increase of enthalpy of reduction and lattice shrinkage, and the Ti site incorporation of acceptor Ca generates $\text{V}_\text{O}^{\bullet\bullet}$ in BaTiO_3 . Fig. 15a and b show the time-dependent IR degradation behavior of Ca-doped BaTiO_3 ($(\text{Ba}_{1-x}\text{Ca}_x)(\text{Ti}_{1-y}\text{Ca}_y)\text{O}_3$) with coarse grains reoxidized in air and with fine grains reoxidized in a N_2 atmosphere at high temperatures under a high DC field, respectively. There is no significant difference in IR degradation behavior with increasing x , whereas IR degradation behavior was accelerated in both coarse- and fine-grained Ca-doped BaTiO_3 as y increased. These results indicate that the IR degradation behavior of Ca-doped BaTiO_3 is significantly affected by the generation of $\text{V}_\text{O}^{\bullet\bullet}$ due to the Ti site incorporation of Ca rather than lattice shrinkage and increase of enthalpy of reduction due to the Ba site incorporation of Ca.

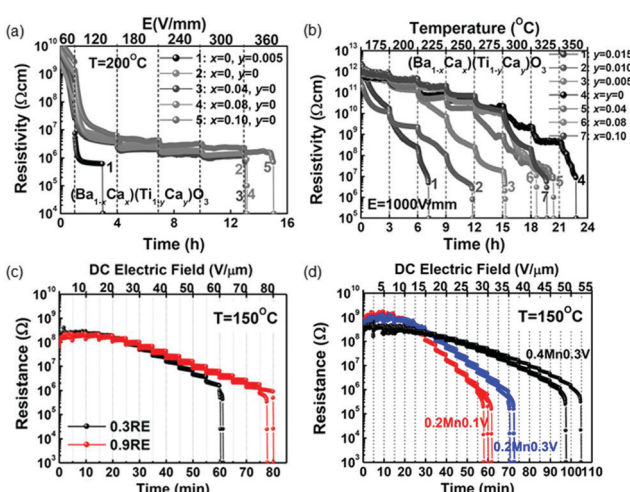


Fig. 15 IR degradation behavior of $(\text{Ba}_{1-x}\text{Ca}_x)\text{TiO}_3$ and $\text{Ba}(\text{Ti}_{1-y}\text{Ca}_y)\text{O}_3$ ceramics with (a) coarse grains that were reoxidized in air and (b) fine grains that were reoxidized in N_2 under a high dc field at $200\text{ }^\circ\text{C}$. Reproduced with permission from ref. 173. (c) Electrical resistivity versus time at $150\text{ }^\circ\text{C}$ under a dc field for 0.4 mol% Mn–0.3 mol% Dy-doped BaTiO_3 and 0.4 mol% Mn–0.9 mol% Dy-doped BaTiO_3 based MLCCs, respectively. Reproduced with permission from ref. 176. (d) Electrical resistivity versus time at $150\text{ }^\circ\text{C}$ under a dc field for 0.2 mol% Mn–0.1 mol% V-doped BaTiO_3 , 0.2 mol% Mn–0.3 mol% V-doped BaTiO_3 and 0.4 mol% Mn–0.3 mol% V-doped BaTiO_3 based MLCC samples, respectively. Reproduced with permission from ref. 177.

It is conventionally believed that MLCCs show nonreducibility and reliability when their dielectric layers are doped with amphoteric dopants of rare earth elements that can occupy the Ba or Ti sites such as Y, Dy, and Ho, and Ti-site variable valence acceptors, such as Mn, Cr, and V. Therefore, some researchers have tried to improve the IR degradation behavior of BaTiO_3 by the co-doping method.^{134,174–177} Fig. 15c shows the time-dependent IR degradation behavior of Dy and Mn-codoped BaTiO_3 systems at a high temperature under various dc fields. The MLCCs based on BaTiO_3 doped with a higher concentration of Dy show the resistance drop under a higher field of $80\text{ V }\mu\text{m}^{-1}$. This result means that BaTiO_3 doped with a higher concentration of rare-earth elements shows a more stable resistance value and endures higher electric field and longer time. The IR degradation behavior of MLCCs can be also improved by co-doping with two types of variable valence acceptors.¹⁷⁷ As shown in Fig. 15d, the MLCCs based on Mn and V-codoped BaTiO_3 systems show more stable and more improved IR degradation behavior with the increase of Mn or V doping concentration. It is attributed to the dominant electron/hole trapping effect due to the multi-valence nature of Mn and V with the increase of Mn or V concentration.

As the dielectric layer of the MLCCs becomes thinner for higher capacities, other factors besides the oxygen vacancy concentration due to doping should be considered to improve IR characteristics. For example, as Zr doping concentration increases, Zr-doped BaTiO_3 bulk ceramics show more stable resistance, longer time and higher electric field for the loss of resistance.¹⁵² In contrast, the MLCCs based on the Zr-doped BaTiO_3 system show no distinct difference in IR degradation behavior with the variation of Zr concentration. The difference in IR degradation behavior between bulk ceramics and MLCCs results from the trapping/detrapping phenomena of charge carriers at trap sites because the dielectric layers in MLCCs experience a much higher electric field. When the concentration of injected charge carriers exceeds the density of trap sites, an abrupt increase of leakage current, which causes IR degradation, occurs. Therefore, in order to improve the reliability of MLCCs, it is necessary to control the trapping/detrapping phenomena of charge carriers at trap sites under a high electric field as well as the $\text{V}_\text{O}^{\bullet\bullet}$ concentration through doping.

For the real application of MLCCs, the IR degradation behavior in a high-humidity environment is also important. Although the IR degradation behavior in the absence of humidity is theoretically well established, the IR degradation behavior in humid conditions has been rarely studied and needs to be clarified. Recently, Saito *et al.* reported the IR degradation mechanism of MLCCs during highly accelerated temperature and humidity stress tests.¹⁷⁸ The authors demonstrated that hydrogen ions generated by H_2O electrolysis at the interface between the dielectric and anode contribute to the IR degradation under humid conditions rather than structural defects, grain growth and the dispersion of additive elements. In order to enhance the reliability and lifetime of MLCCs, it can be known that the operating conditions of MLCCs, such as temperature, voltage and humidity, have to be considered.

4.9. Interface between BaTiO₃ dielectric layers and base metal electrodes

After lamination, the green MLCCs are sintered at high temperature (> 1200 °C). Due to high temperature, Ni from inner metal electrodes is diffused into BaTiO₃ dielectric layers. Therefore, many researchers have investigated the Ni/BaTiO₃ interface using various techniques such as XPS, TEM and X-ray nanotomography.^{179–181} When Ni diffusion into the BaTiO₃ dielectric layer occurs, oxygen vacancies are generated, resulting in a decrease of electron conduction. However, IR degradation behavior becomes poor due to the migration of oxygen vacancies under dc bias.¹⁸² In addition, due to the different shrinkage behavior between Ni and BaTiO₃, Ni inner electrodes show severe discontinuities during sintering.¹⁸³ The shrinkage behavior can be alleviated by adding an amount of BaTiO₃ into Ni and using the powder with small particle size.¹⁷⁹

As Ni can be easily oxidized, green MLCCs are sintered at low oxygen pressure. However, the reductive atmosphere generates a large amount of oxygen vacancies in BaTiO₃, resulting in its insulation resistance and lifetime drop. In order to decrease the oxygen vacancies, a reoxidation process, annealing at a relatively oxidizing atmosphere, is performed. It is important to precisely control the sintering atmosphere to maintain the high electrical conductivity of Ni and to reduce the number of oxygen vacancies in BaTiO₃.^{184–186} When Ni inks are mixed with Li₂CO₃, Ni can preserve the electrical conductivity even though the MLCCs were sintered in a higher partial pressure of oxygen.¹⁸⁶ Moreover, the leakage current of MLCCs decreases due to the higher activation energy of the electrode interface and the reoxidation process under a higher partial pressure of oxygen. Therefore, the

interface between BaTiO₃ dielectric layers and Ni inner electrodes should be controlled for the higher performance and reliability of MLCCs.

5. Outlook and conclusion

Until now, MLCCs have been utilized for various different applications such as televisions, personal computers, communications, mobile phones, and electric vehicles. Furthermore, with the advent of the Internet of Things (IoT), their application has become much broader now. In this review, we summarized the current issues and recent progress in developing MLCCs with high capacitance and reliability from a viewpoint of designing dielectric materials, especially BaTiO₃. With the trend toward miniaturization, higher performance and high volumetric-efficiency, the thickness of dielectric layers in MLCCs has become lower and stacking more dielectric layers is necessary. Therefore, finer dielectric powder and a thin dielectric layer with smaller grain size are needed, but inevitably the permittivity of the dielectric layer decreases. IR degradation behavior and dielectric nonlinearity depending on temperature, frequency, and dc bias also deteriorate the reliability of MLCCs (Fig. 16).

These limits and issues of conventional MLCCs can be solved by the rational design of BaTiO₃ dielectric layers including nano/microstructure control, doping and surface modification. For example, rare earth elements can significantly change the dielectric properties of BaTiO₃ as they can affect the growth of the BaTiO₃ nano/microstructure, tetragonality and defect generation, which are related with the reliability and performance of MLCCs. The change in nano/microstructure and tetragonality is

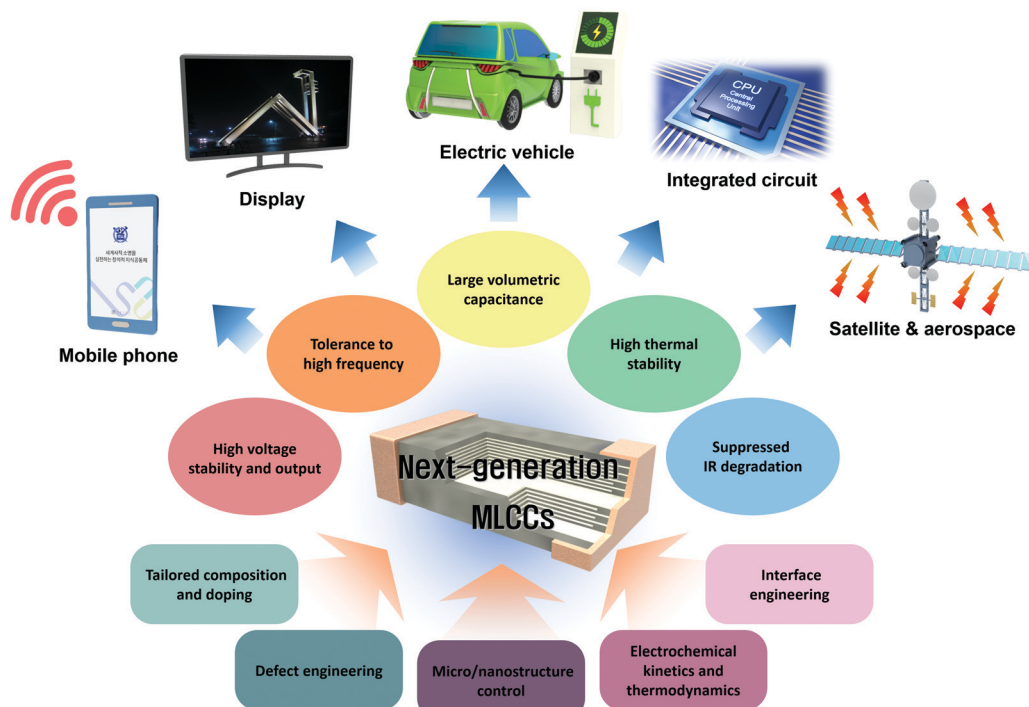


Fig. 16 Schematic of MLCCs with critical issues in developing high performance and reliable MLCCs and their various applications.

directly related to the dielectric permittivity of BaTiO₃, which is critical for the capacitance of MLCCs. The choice of a suitable dopant can contribute to the improved thermal reliability and Curie temperature control. With the defect engineering of BaTiO₃, the degradation behaviour of MLCCs can be suppressed. In addition, as base metals are mainly used as inner electrodes, fine control of process conditions, such as sintering under a reducing atmosphere and reoxidation, should be also considered. Therefore, it can be concluded that a comprehensive and careful understanding of the electrochemical kinetics and thermodynamics of BaTiO₃ is needed for developing high performance and reliable MLCCs, as they can change the overall dielectric properties.

Recently, decreasing the thickness of the chip itself, known as the low-profile MLCC, has been actively investigated, as there is limited space for MLCCs in portable devices, such as smartphones and tablet PCs. Low-profile MLCCs are mainly used in semiconductor packages and camera modules. Embedded MLCCs have been also developed and mass-produced in case the mounting space for MLCCs is no longer available. The difference between embedded MLCCs and conventional MLCCs is that there is no electroplating layer for soldering in embedded MLCCs. For better connection with the circuit, the terminal electrode width of embedded MLCCs should be precisely controlled. In addition, there has been growing interest in MLCCs for automotive applications. To operate in harsh conditions, MLCCs should withstand high voltage, temperature, and humidity. Particularly, MLCCs for automotive application are required to have high bending strength characteristics. The demand for MLCCs with a low equivalent series inductance (ESL) has also increased due to the steep increase of clock frequency in the IC of recent electronic devices. Because conventional MLCCs have a high ESL in the frequency level of GHz, there is a limit in the impedance matching for noise cancelling. As known from the development trends, novel platforms to meet the needs of the industry as well as improving the performance and reliability of MLCCs are also essential.

Conflicts of interest

There are no conflict to declare.

Acknowledgements

This work was financially supported by the Basic Research Laboratory of NRF (2018R1A4A1022647), the Future Material Discovery Program (2016M3D1A1027666, 2018M3D1A1058793) and the Basic Science Research Program (2017R1A2B3009135) from the Ministry of Science and ICT and the BK21 PLUS SNU Materials Division for Educating Creative Global Leaders (21A20131912052) from the Ministry of Education through the National Research Foundation of Korea.

References

- H. Hao, M. Liu, H. Liu, S. Zhang, X. Shu, T. Wang, Z. Yao and M. Cao, *RSC Adv.*, 2015, **5**, 8868–8876.
- Y. Zhang, X. Wang, J.-Y. Kim, Z. Tian, J. Fang, K.-H. Hur and L. Li, *J. Am. Ceram. Soc.*, 2012, **95**, 1628–1633.
- H. Kishi, Y. Mizuno and H. Chazono, *Jpn. J. Appl. Phys.*, 2003, **42**, 1–15.
- C. Pithan, D. Hennings and R. Waser, *Int. J. Appl. Ceram. Technol.*, 2005, **2**, 1–14.
- Samsung Electro-Mechanics, http://www.samsungsem.com/global/news/cardnews/1450267_4619.jsp, accessed May 2019.
- Chlue Research, <http://www.chlueresearch.com/downloads/global-mlcc-ceramic-powder-market-report-2017-pdf>, accessed May 2019.
- T. Hoshina, *J. Ceram. Soc. Jpn.*, 2013, **121**, 156–161.
- S.-H. Yoon, J.-S. Park, C.-H. Kim and D.-Y. Kim, *J. Appl. Phys.*, 2014, **115**, 244101.
- S.-H. Yoon, C. A. Randall and K.-H. Hur, *J. Am. Ceram. Soc.*, 2009, **92**, 2944–2952.
- R. M. Waser, *J. Am. Ceram. Soc.*, 1989, **72**, 2234–2240.
- D. F. K. Hennings and H. Schreinemacher, *J. Eur. Ceram. Soc.*, 1995, **15**, 795–800.
- R. W. Johnson, J. L. Evans, P. Jacobsen, J. R. Thompson and M. Christopher, *IEEE Trans. Electron. Packag. Manuf.*, 2004, **27**, 164–176.
- S.-J. Lee, K.-Y. Kang and S.-K. Han, *Appl. Phys. Lett.*, 1999, **75**, 1784–1786.
- K. Hong, T. H. Lee, J. M. Suh, J.-S. Park, H.-S. Kwon, J. Choi and H. W. Jang, *Electron. Mater. Lett.*, 2018, **14**, 629–635.
- H. Kishi, N. Kohzu, Y. Mizuno, Y. Iguchi, J. Sugino, H. Ohsato and T. Okuda, *Jpn. J. Appl. Phys.*, 1999, **38**, 5452–5456.
- J. Gao, Y. Wang, Y. Liu, X. Hu, X. Ke, L. Zhong, Y. He and X. Ren, *Sci. Rep.*, 2017, **7**, 40916.
- S. Dwivedi, T. Pareek and S. Kumar, *RSC Adv.*, 2018, **8**, 24286–24296.
- X. Jiang, F. Tang, J. T. Wang and T. P. Chen, *Physica C*, 2001, **364–365**, 678–683.
- S. Zhang, J. Luo, W. Hackenberger, N. P. Sherlock, R. J. Meyer Jr. and T. R. Shrout, *J. Appl. Phys.*, 2009, **105**, 104506.
- B. Sundarakannan, K. Kakimoto and H. Ohsato, *J. Appl. Phys.*, 2003, **94**, 5182–5187.
- V. G. Bhide, K. G. Deshmukh and M. S. Hegde, *Physica*, 1962, **28**, 871–876.
- L. Luo, B. Wang, X. Jiang and W. Li, *J. Mater. Sci.*, 2014, **49**, 1659–1665.
- J. T. Zeng, K. W. Kwok and H. L. W. Chan, *J. Am. Ceram. Soc.*, 2006, **89**, 2828–2832.
- X. Hao, J. Zhai and X. Yao, *J. Am. Ceram. Soc.*, 2009, **92**, 1133–1135.
- T. M. Correia, M. McMillen, M. K. Rokosz, P. M. Weaver, J. M. Gregg, G. Viola and M. G. Cain, *J. Am. Ceram. Soc.*, 2013, **96**, 2699–2702.
- Z. Li, J. Wang, X. Wang, Q. Yang and Z. Zhang, *RSC Adv.*, 2015, **5**, 80950–80955.
- J. Li, X. Hu, G. Gao, S. Ding, H. Li, L. Yang and Z. Zhang, *J. Mater. Chem. C*, 2013, **1**, 1111–1121.
- T. Basu, S. Sen, A. Seal and A. Sen, *J. Electron. Mater.*, 2016, **45**, 2252–2257.

- 29 L. Liu, S. Zheng, Y. Huang, D. Shi, S. Wu, L. Fang, C. Hu and B. Elouadi, *J. Phys. D: Appl. Phys.*, 2012, **45**, 295403.
- 30 X. Liu, L. Liu, F. Han, S. Liu, H. Xiang and L. Fang, *J. Mater. Sci.: Mater. Electron.*, 2016, **27**, 12128–12133.
- 31 M. Xu, B. Peng, J. Zhu, L. Liu, W. Sun, G. J. T. Leighton, C. Shaw, N. Luo and Q. Zhang, *J. Alloys Compd.*, 2019, **789**, 303–312.
- 32 J. Li, F. Li, Z. Xu and S. Zhang, *Adv. Mater.*, 2018, **30**, 1802155.
- 33 A. J. Moulson and J. M. Herbert, *Electroceramics: materials, properties, applications*, John Wiley & Sons, 2003.
- 34 M. Aghayan, A. Khorsand Zak, M. Behdani and A. Manaf Hashim, *Ceram. Int.*, 2014, **40**, 16141–16146.
- 35 D. Hennings and G. Rosenstein, *J. Am. Ceram. Soc.*, 1984, **67**, 249–254.
- 36 Y. Park and H. G. Kim, *Ceram. Int.*, 1997, **23**, 329–336.
- 37 M. Pan and C. A. Randall, *IEEE Electr. Insul. Mag.*, 2010, **26**, 44–50.
- 38 S.-H. Yoon, S.-H. Kim and D.-Y. Kim, *J. Appl. Phys.*, 2013, **114**, 074102.
- 39 T. Tsurumi, H. Adachi, H. Kakemoto, S. Wada, Y. Mizuno, H. Chazono and H. Kishi, *Jpn. J. Appl. Phys.*, 2002, **41**, 6929–6933.
- 40 H. Chazono and H. Kishi, *Key Eng. Mater.*, 2001, **216**, 47–52.
- 41 T. Hoshina, S. Wada, Y. Kuroiwa and T. Tsurumi, *Appl. Phys. Lett.*, 2008, **93**, 192914.
- 42 T. Yan, Z.-G. Shen, W.-W. Zhang and J.-F. Chen, *Mater. Chem. Phys.*, 2006, **98**, 450–455.
- 43 K. Ishikawa and T. Uemori, *Phys. Rev. B: Condens. Matter Mater. Phys.*, 1999, **60**, 11841–11845.
- 44 D. Damjanovic, *Rep. Prog. Phys.*, 1998, **61**, 1267–1324.
- 45 W. Buessem, L. Cross and A. Goswami, *J. Am. Ceram. Soc.*, 1966, **49**, 33–36.
- 46 G. Arlt, D. Hennings and G. d. With, *J. Appl. Phys.*, 1985, **58**, 1619–1625.
- 47 G. Arlt and N. A. Pertsev, *J. Appl. Phys.*, 1991, **70**, 2283–2289.
- 48 R. Waser, *Integr. Ferroelectr.*, 1997, **15**, 39–51.
- 49 S.-H. Yoon, S.-J. Kim, S.-H. Kim and D.-Y. Kim, *J. Appl. Phys.*, 2013, **114**, 224103.
- 50 C. R. Pike, A. P. Roberts and K. L. Verosub, *J. Appl. Phys.*, 1999, **85**, 6660–6667.
- 51 F. Béron, L. A. Valenzuela, M. Knobel, L. G. C. Melo and K. R. Pirota, *J. Magn. Magn. Mater.*, 2012, **324**, 1601–1605.
- 52 Y.-M. Chiang and T. Takagi, *J. Am. Ceram. Soc.*, 1990, **73**, 3278–3285.
- 53 R. Hagenbeck, L. Schneider-Störmann, M. Vollmann and R. Waser, *Mater. Sci. Eng., B*, 1996, **39**, 179–187.
- 54 S. H. Yoon and H. Kim, *J. Mater. Res.*, 2001, **16**, 1479–1486.
- 55 Z. Tian, X. Wang, H. Gong, T.-H. Song, K. H. Hur and L. Li, *J. Am. Ceram. Soc.*, 2011, **94**, 973–977.
- 56 S.-H. Yoon, M.-Y. Kim, C.-H. Nam, J.-W. Seo, S.-K. Wi and K.-H. Hur, *Appl. Phys. Lett.*, 2015, **107**, 072906.
- 57 K. Watanabe, I. Sakaguchi, S. Hishita, N. Ohashi and H. Haneda, *Appl. Phys. Express*, 2011, **4**, 055801.
- 58 T. Oyama, N. Wada, H. Takagi and M. Yoshiya, *Phys. Rev. B: Condens. Matter Mater. Phys.*, 2010, **82**, 134107.
- 59 H. Gong, X. Wang, S. Zhang, H. Wen and L. Li, *J. Eur. Ceram. Soc.*, 2014, **34**, 1733–1739.
- 60 X. Wei, G. Xu, Z. Ren, G. Shen and G. Han, *J. Am. Ceram. Soc.*, 2008, **91**, 3774–3780.
- 61 X. Zhu, J. Zhu, S. Zhou, Z. Liu, N. Ming and D. Hesse, *J. Cryst. Growth*, 2005, **283**, 553–562.
- 62 J.-O. Hong, S.-H. Kim and K.-H. Hur, *J. Korean Ceram. Soc.*, 2009, **46**, 161.
- 63 P. P. Phule and S. H. Risbud, *J. Mater. Sci.*, 1990, **25**, 1169–1183.
- 64 N. Bao, L. Shen, A. Gupta, A. Tatarenko, G. Srinivasan and K. Yanagisawa, *Appl. Phys. Lett.*, 2009, **94**, 253109.
- 65 S. Adireddy, C. Lin, B. Cao, W. Zhou and G. Caruntu, *Chem. Mater.*, 2010, **22**, 1946–1948.
- 66 W. Zhang, S. Li, H. Ma, D. Hu, X. Kong, S. Uemura, T. Kusunose and Q. Feng, *Nanoscale*, 2019, **11**, 3837–3846.
- 67 S.-O. Kang, H.-S. Jang, K.-B. Kim, B. H. Park, M.-J. Jung and Y.-I. Kim, *Mater. Res. Bull.*, 2008, **43**, 996–1003.
- 68 K.-C. Huang, T.-C. Huang and W.-F. Hsieh, *Inorg. Chem.*, 2009, **48**, 9180–9184.
- 69 B. Jiang, J. Iocozzia, L. Zhao, H. Zhang, Y.-W. Harn, Y. Chen and Z. Lin, *Chem. Soc. Rev.*, 2019, **48**, 1194–1228.
- 70 I. Fujii, M. Ugorek and S. Trolier-McKinstry, *J. Appl. Phys.*, 2010, **107**, 104116.
- 71 N. B. Gharb and S. Trolier-McKinstry, *J. Appl. Phys.*, 2005, **97**, 064106.
- 72 T. Tsurumi, M. Shono, H. Kakemoto, S. Wada, K. Saito and H. Chazono, *Jpn. J. Appl. Phys.*, 2005, **44**, 6989–6994.
- 73 S. Lee, G. A. Rossetti Jr., Z.-K. Liu and C. A. Randall, *J. Appl. Phys.*, 2009, **105**, 093519.
- 74 C.-Y. Chang, R.-L. Wang and C.-Y. Huang, *J. Mater. Res.*, 2012, **27**, 2937–2942.
- 75 M. T. Buscaglia, M. Viviani, V. Buscaglia, C. Bottino and P. Nanni, *J. Am. Ceram. Soc.*, 2002, **85**, 1569–1575.
- 76 W.-H. Lee, T.-Y. Tseng and D. Hennings, *J. Mater. Sci.: Mater. Electron.*, 2000, **11**, 157–162.
- 77 H. Saito, H. Chazono, H. Kishi and N. Yamaoka, *Jpn. J. Appl. Phys.*, 1991, **30**, 2307–2310.
- 78 L. Liu, S. Ren, J. Zhang, B. Peng, L. Fang and D. Wang, *J. Am. Ceram. Soc.*, 2018, **101**, 2408–2416.
- 79 G. Schileo, A. Feteira, K. Reichmann, M. Li and D. C. Sinclair, *J. Eur. Ceram. Soc.*, 2015, **35**, 2479–2488.
- 80 Y.-C. Lee and C.-S. Chiang, *J. Alloys Compd.*, 2011, **509**, 6973–6979.
- 81 F. Batllo, E. Duverger, J.-C. Jules, J.-C. Niepce, B. Jannot and M. Maglione, *Ferroelectrics*, 1990, **109**, 113–118.
- 82 X. W. Zhang, Y. H. Han, M. Lal and D. M. Smyth, *J. Am. Ceram. Soc.*, 1987, **70**, 100–103.
- 83 T.-T. Fang and J.-T. Shuei, *J. Mater. Res.*, 1999, **14**, 1910–1915.
- 84 H. Gong, X. Wang, S. Zhang, Z. Tian and L. Li, *J. Appl. Phys.*, 2012, **112**, 114119.
- 85 K. Morita, Y. Mizuno, H. Chazono and H. Kishi, *Jpn. J. Appl. Phys.*, 2002, **41**, 6957–6961.
- 86 H.-W. Lee, M. S. H. Chu and H.-Y. Lu, *J. Am. Ceram. Soc.*, 2009, **92**, 3037–3043.

- 87 S. K. Jo, J. S. Park and Y. H. Han, *J. Alloys Compd.*, 2010, **501**, 259–264.
- 88 G. Yao, X. Wang, Y. Yang and L. Li, *J. Am. Ceram. Soc.*, 2010, **93**, 1697–1701.
- 89 H. Kishi, N. Kohzu, J. Sugino, H. Ohsato, Y. Iguchi and T. Okuda, *J. Eur. Ceram. Soc.*, 1999, **19**, 1043–1046.
- 90 R. D. Shannon, *Acta Crystallogr., Sect. A: Cryst. Phys., Diff., Theor. Gen. Crystallogr.*, 1976, **32**, 751–767.
- 91 Y. Mizuno, H. Kishi, K. Ohnuma, T. Ishikawa and H. Ohsato, *J. Eur. Ceram. Soc.*, 2007, **27**, 4017–4020.
- 92 Y. Li, Y. Hao, X. Wang and X. Yao, *Ferroelectrics*, 2010, **407**, 134–139.
- 93 H. Gong, X. Wang, S. Zhang and L. Li, *Mater. Res. Bull.*, 2016, **73**, 233–239.
- 94 Y.-X. Li, X. Yao, X.-S. Wang and Y.-B. Hao, *Ceram. Int.*, 2012, **38**, S29–S32.
- 95 D. W. Kang, T. G. Park, J. W. Kim, J. S. Kim, H. S. Lee and H. Cho, *Electron. Mater. Lett.*, 2010, **6**, 145–149.
- 96 V. V. Mitic, Z. S. Nikolic, V. B. Pavlovic, V. Paunovic, M. Miljkovic, B. Jordovic and L. Zivkovic, *J. Am. Ceram. Soc.*, 2010, **93**, 132–137.
- 97 S. Zheng, D. Shi, L. Liu, G. Li, Q. Wang, L. Fang and B. Elouadi, *J. Mater. Sci.: Mater. Electron.*, 2014, **25**, 4058–4065.
- 98 J. Kim, D. Kim, J. Kim, Y.-n. Kim, K. N. Hui and H. Lee, *Electron. Mater. Lett.*, 2011, **7**, 155–159.
- 99 D. I. Spang, I. Burn and A. Safari, *IEEE*, 1996, 809–812.
- 100 Y. Li, X. Yao, X. Wang and L. Zhang, *Ferroelectrics*, 2009, **384**, 73–78.
- 101 L. Zhang, O. P. Thakur, A. Feteira, G. M. Keith, A. G. Mould, D. C. Sinclair and A. R. West, *Appl. Phys. Lett.*, 2007, **90**, 142914.
- 102 T. Mitsui and W. B. Westphal, *Phys. Rev.*, 1961, **124**, 1354–1359.
- 103 Z. Q. Zhuang, M. P. Harmer, D. M. Smyth and R. E. Newnham, *Mater. Res. Bull.*, 1987, **22**, 1329–1335.
- 104 Y. H. Han, J. B. Appleby and D. M. Smyth, *J. Am. Ceram. Soc.*, 1987, **70**, 96–100.
- 105 C. Fu, N. Chen and G. Du, *Ceram. Int.*, 2017, **43**, 15927–15931.
- 106 S. K. Das, R. N. Mishra and B. K. Roul, *Solid State Commun.*, 2014, **191**, 19–24.
- 107 G.-P. Du, Z.-J. Hu, Q.-F. Han, X.-M. Qin and W.-Z. Shi, *J. Alloys Compd.*, 2010, **492**, L79–L81.
- 108 H. T. Langhammer, T. Müller, R. Böttcher and H. P. Abicht, *J. Phys.: Condens. Matter*, 2008, **20**, 085206.
- 109 Y. Li, Q. Liu, T. Yao, Z. Pan, Z. Sun, Y. Jiang, H. Zhang, Z. Pan, W. Yan and S. Wei, *Appl. Phys. Lett.*, 2010, **96**, 091905.
- 110 Murata, <https://www.murata.com/ko-kr/about/rd/material-development>, accessed May 2019.
- 111 S.-H. Yoon, Y. Park, C.-H. Kim and D.-Y. Kim, *Appl. Phys. Lett.*, 2014, **105**, 242902.
- 112 L. Liu and H. Fan, *J. Electroceram.*, 2006, **16**, 293–296.
- 113 L. Liu, H. Fan, S. Ke and X. Chen, *J. Alloys Compd.*, 2008, **458**, 504–508.
- 114 L. Liu, M. Knapp, H. Ehrenberg, L. Fang, L. A. Schmitt, H. Fuess, M. Hoelzel and M. Hinterstein, *J. Appl. Crystallogr.*, 2016, **49**, 574–584.
- 115 L. Liu, M. Knapp, L. A. Schmitt, H. Ehrenberg, L. Fang, H. Fuess, M. Hoelzel and M. Hinterstein, *Europhys. Lett.*, 2016, **114**, 47011.
- 116 L. Liu, M. Knapp, H. Ehrenberg, L. Fang, H. Fan, L. A. Schmitt, H. Fuess, M. Hoelzel, H. Dammak, M. P. Thi and M. Hinterstein, *J. Eur. Ceram. Soc.*, 2017, **37**, 1387–1399.
- 117 L. Liu, X. Ma, M. Knapp, H. Ehrenberg, B. Peng, L. Fang and M. Hinterstein, *Europhys. Lett.*, 2017, **118**, 47001.
- 118 M. Wu, L. Fang, L. Liu, G. Li and B. Elouadi, *Ferroelectrics*, 2015, **478**, 18–25.
- 119 F. Han, J. Deng, X. Liu, T. Yan, S. Ren, X. Ma, S. Liu, B. Peng and L. Liu, *Ceram. Int.*, 2017, **43**, 5564–5573.
- 120 L. Li, M. Xu, Q. Zhang, P. Chen, N. Wang, D. Xiong, B. Peng and L. Liu, *Ceram. Int.*, 2018, **44**, 343–350.
- 121 L. Liu, D. Shi, M. Knapp, H. Ehrenberg, L. Fang and J. Chen, *J. Appl. Phys.*, 2014, **116**, 184104.
- 122 S. Zheng, E. Odendo, L. Liu, D. Shi, Y. Huang, L. Fan, J. Chen, L. Fang and B. Elouadi, *J. Appl. Phys.*, 2013, **113**, 094102.
- 123 S. Zheng, L. Fan, E. Odendo, L. Liu, D. Shi, G. Li, J. Chen, L. Fang and B. Elouadi, *Curr. Appl. Phys.*, 2014, **14**, 13–17.
- 124 S. Ren, Z. Chen, T. Yan, F. Han, X. Kuang, L. Fang and L. Liu, *J. Phys. Chem. Solids*, 2018, **118**, 99–108.
- 125 J. Wang, S. Jiang, D. Jiang, J. Tian, Y. Li and Y. Wang, *Ceram. Int.*, 2012, **38**, 5853–5857.
- 126 W.-H. Lee and C.-Y. Su, *J. Am. Ceram. Soc.*, 2007, **90**, 3345–3348.
- 127 Y. Yuan, S. R. Zhang, X. H. Zhou, B. Tang and B. Li, *J. Electron. Mater.*, 2009, **38**, 706–710.
- 128 D. H. Choi, A. Baker, M. Lanagan, S. Trolier-McKinstry and C. Randall, *J. Am. Ceram. Soc.*, 2013, **96**, 2197–2202.
- 129 D. S. Tinberg and S. Trolier-McKinstry, *J. Appl. Phys.*, 2007, **101**, 024112.
- 130 H. Ogihara, C. A. Randall and S. Trolier-McKinstry, *J. Am. Ceram. Soc.*, 2009, **92**, 110–118.
- 131 N. Kumar, A. Ionin, T. Ansell, S. Kwon, W. Hackenberger and D. Cann, *Appl. Phys. Lett.*, 2015, **106**, 252901.
- 132 L. Ben and D. C. Sinclair, *Appl. Phys. Lett.*, 2011, **98**, 092907.
- 133 Y. Liu and A. R. West, *J. Eur. Ceram. Soc.*, 2009, **29**, 3249–3257.
- 134 B. Zhang and L. Li, *RSC Adv.*, 2016, **6**, 24518–24526.
- 135 A. S. Shaikh and R. W. Vest, *J. Am. Ceram. Soc.*, 1986, **69**, 689–694.
- 136 F. D. Morrison, A. M. Coats, D. C. Sinclair and A. R. West, *J. Electroceram.*, 2001, **6**, 219–232.
- 137 Z. Jing, Z. Yu and C. Ang, *J. Mater. Res.*, 2002, **17**, 2787–2793.
- 138 T. Sun, X. Wang, H. Wang, Z. Cheng, X. Zhang and L. Li, *J. Am. Ceram. Soc.*, 2010, **93**, 3808–3813.
- 139 S.-H. Yoon, M.-Y. Kim and D. Kim, *J. Appl. Phys.*, 2017, **122**, 154103.
- 140 T. Tsurumi, M. Shono, H. Kakemoto, S. Wada, K. Saito and H. Chazono, *J. Electroceram.*, 2008, **21**, 17–21.

- 141 T. Nomura, N. Kawano, J. Yamamoto, T. Arashi, Y. Nakano and A. Sato, *Jpn. J. Appl. Phys.*, 1995, **34**, 5389–5395.
- 142 Y. K. Vayunandana Reddy and D. Mergel, *Physica B*, 2007, **391**, 212–221.
- 143 S. Liu, L. Huang, J. Li and S. O'Brien, *J. Appl. Phys.*, 2012, **112**, 014108.
- 144 S.-H. Yoon, S.-H. Kwon and K.-H. Hur, *J. Appl. Phys.*, 2011, **109**, 084117.
- 145 J. Jamnik and J. Maier, *J. Electrochem. Soc.*, 1999, **146**, 4183–4188.
- 146 J. Jamnik and J. Maier, *Phys. Chem. Chem. Phys.*, 2001, **3**, 1668–1678.
- 147 N. J. Kidner, N. H. Perry, T. O. Mason and E. J. Garboczi, *J. Am. Ceram. Soc.*, 2008, **91**, 1733–1746.
- 148 M. H. Khan, S. Pal and E. Bose, *Appl. Phys. A: Mater. Sci. Process.*, 2015, **118**, 907–912.
- 149 T. Tsurumi, J. Li, T. Hoshina, H. Kakemoto, M. Nakada and J. Akedo, *Appl. Phys. Lett.*, 2007, **91**, 182905.
- 150 J.-K. Chun and H.-I. Yoo, *J. Korean Ceram. Soc.*, 2012, **49**, 48–55.
- 151 S.-H. Yoon, C. A. Randall and K.-H. Hur, *J. Am. Ceram. Soc.*, 2010, **93**, 1950–1956.
- 152 S.-H. Yoon, J.-R. Kim, S.-H. Yoon, C.-H. Kim and D.-Y. Kim, *J. Mater. Res.*, 2013, **28**, 1078–1086.
- 153 G. Y. Yang, E. C. Dickey, C. A. Randall, D. E. Barber, P. Pinceloup, M. A. Henderson, R. A. Hill, J. J. Beeson and D. J. Skamser, *J. Appl. Phys.*, 2004, **96**, 7492–7499.
- 154 G. Y. Yang, G. D. Lian, E. C. Dickey, C. A. Randall, D. E. Barber, P. Pinceloup, M. A. Henderson, R. A. Hill, J. J. Beeson and D. J. Skamser, *J. Appl. Phys.*, 2004, **96**, 7500–7508.
- 155 C. A. Randall, R. Maier, W. Qu, K. Kobayashi, K. Morita, Y. Mizuno, N. Inoue and T. Oguni, *J. Appl. Phys.*, 2013, **113**, 014101.
- 156 K. Morita, T. Shimura, S. Abe and Y. Konishi, *Jpn. J. Appl. Phys.*, 2018, **57**, 11UC03.
- 157 M. Vollmann and R. Waser, *J. Electroceram.*, 1997, **1**, 51–64.
- 158 R. Waser and R. Hagenbeck, *Acta Mater.*, 2000, **48**, 797–825.
- 159 D. F. K. Hennings, *J. Eur. Ceram. Soc.*, 2001, **21**, 1637–1642.
- 160 Y. Tsur, T. D. Dunbar and C. A. Randall, *J. Electroceram.*, 2001, **7**, 25–34.
- 161 C. A. Randall, *J. Ceram. Soc. Jpn.*, 2001, **109**, S2–S6.
- 162 Y. Sakabe, Y. Hamaji, H. Sano and N. Wada, *Jpn. J. Appl. Phys.*, 2002, **41**, 5668–5673.
- 163 S.-H. Yoon, C. A. Randall and K.-H. Hur, *J. Am. Ceram. Soc.*, 2009, **92**, 1758–1765.
- 164 S.-H. Yoon, C. A. Randall and K.-H. Hur, *J. Am. Ceram. Soc.*, 2009, **92**, 1766–1772.
- 165 D.-Y. Lu and Y. Liang, *Ceram. Int.*, 2018, **44**, 14717–14727.
- 166 Y.-Y. Yeoh, H. Jang and H.-I. Yoo, *Phys. Chem. Chem. Phys.*, 2012, **14**, 1642–1648.
- 167 H.-I. Yoo, T.-S. Oh, H.-S. Kwon, D.-K. Shin and J.-S. Lee, *Phys. Chem. Chem. Phys.*, 2009, **11**, 3115–3126.
- 168 S.-H. Yoon, C. A. Randall and K.-H. Hur, *J. Appl. Phys.*, 2010, **108**, 064101.
- 169 H.-J. Hagemann and D. Hennings, *J. Am. Ceram. Soc.*, 1981, **64**, 590–594.
- 170 C.-R. Song, H.-I. Yoo and J.-Y. Kim, *J. Electroceram.*, 1997, **1**, 27–39.
- 171 D. K. Lee, H. I. Yoo and K. D. Becker, *Solid State Ionics*, 2002, **154–155**, 189–193.
- 172 R. Merkle and J. Maier, *Phys. Chem. Chem. Phys.*, 2003, **5**, 2297–2303.
- 173 S.-H. Yoon, S.-H. Kang, S.-H. Kwon and K.-H. Hur, *J. Mater. Res.*, 2010, **25**, 2135–2142.
- 174 M. C. Ferrarelli, C. C. Tan and D. C. Sinclair, *J. Mater. Chem.*, 2011, **21**, 6292–6299.
- 175 Y. Tsur, A. Hitomi, I. Scrymgeour and C. A. Randall, *Jpn. J. Appl. Phys.*, 2001, **40**, 255–258.
- 176 S.-H. Yoon, J.-B. Lim, S.-H. Kim and D.-Y. Kim, *J. Mater. Res.*, 2013, **28**, 3252–3256.
- 177 S.-H. Yoon, J.-S. Park, S.-H. Kim and D.-Y. Kim, *Appl. Phys. Lett.*, 2013, **103**, 042901.
- 178 Y. Saito, T. Nakamura, K. Nada and H. Sano, *Jpn. J. Appl. Phys.*, 2018, **57**, 11UC04.
- 179 J.-H. Kang, D. Joo, H.-M. Cha, Y.-G. Jung and U. Paik, *Ceram. Int.*, 2008, **34**, 1487–1494.
- 180 D. M. Long, A. Klein and E. C. Dickey, *Appl. Surf. Sci.*, 2019, **466**, 472–476.
- 181 K.-H. Lee, Y.-C. Wu and H.-Y. Lu, *J. Phys. D: Appl. Phys.*, 2007, **40**, 4902–4909.
- 182 H. Gong, X. Wang, Z. Tian, H. Zhang and L. Li, *Electron. Mater. Lett.*, 2014, **10**, 417–421.
- 183 A. V. Polotai, G.-Y. Yang, E. C. Dickey and C. A. Randall, *J. Am. Ceram. Soc.*, 2007, **90**, 3811–3817.
- 184 M. R. Opitz, K. Albertsen, J. J. Beeson, D. F. Hennings, J. L. Routbort and C. A. Randall, *J. Am. Ceram. Soc.*, 2003, **86**, 1879–1884.
- 185 C. C. Lin, W. C. J. Wei, C. Y. Su and C. H. Hsueh, *J. Alloys Compd.*, 2009, **485**, 653–659.
- 186 D. S. B. Heidary and C. A. Randall, *ACS Appl. Mater. Interfaces*, 2016, **8**, 31449–31459.